

SANDIA REPORT

SAND2023-03905

Printed May 2023



Sandia
National
Laboratories

Design and Characterization of a Lens-Coupled System for Dynamic X-Ray Diffraction

Anthony Smith, Tommy Ao

Prepared by
Sandia National Laboratories
Albuquerque, New Mexico 87185
Livermore, California 94550

Issued by Sandia National Laboratories, operated for the United States Department of Energy by National Technology & Engineering Solutions of Sandia, LLC.

NOTICE: This report was prepared as an account of work sponsored by an agency of the United States Government. Neither the United States Government, nor any agency thereof, nor any of their employees, nor any of their contractors, subcontractors, or their employees, make any warranty, express or implied, or assume any legal liability or responsibility for the accuracy, completeness, or usefulness of any information, apparatus, product, or process disclosed, or represent that its use would not infringe privately owned rights. Reference herein to any specific commercial product, process, or service by trade name, trademark, manufacturer, or otherwise, does not necessarily constitute or imply its endorsement, recommendation, or favoring by the United States Government, any agency thereof, or any of their contractors or subcontractors. The views and opinions expressed herein do not necessarily state or reflect those of the United States Government, any agency thereof, or any of their contractors.

Printed in the United States of America. This report has been reproduced directly from the best available copy.

Available to DOE and DOE contractors from

U.S. Department of Energy
Office of Scientific and Technical Information
P.O. Box 62
Oak Ridge, TN 37831

Telephone: (865) 576-8401
Facsimile: (865) 576-5728
E-Mail: reports@osti.gov
Online ordering: <http://www.osti.gov/scitech>

Available to the public from

U.S. Department of Commerce
National Technical Information Service
5301 Shawnee Road
Alexandria, VA 22312

Telephone: (800) 553-6847
Facsimile: (703) 605-6900
E-Mail: orders@ntis.gov
Online order: <https://classic.ntis.gov/help/order-methods>



Design and Characterization of a Lens-Coupled System for Dynamic X-Ray Diffraction

Anthony Smith, Tommy Ao

SAND2023-03905

ABSTRACT

X-ray diffraction (XRD) is a necessary technique for understanding states of materials under static and dynamic loading conditions. The higher-pressure Equation of State (EOS) of many materials can only be explored via shock or ramp compression at temperatures and pressures of interest. While static XRD work has yielded EOS measurements in the 100 - 200 GPa regime, dynamic X-ray diffraction (DXRD) can explore EOS phases in the TPa regime, which closely resembles inner-core planetary conditions. DXRD hinges on the ability to measure the exact phase or phase change of a material while under dynamic loading conditions. Macroscopic diagnostic systems (e.g. velocimetry and pyrometry) can infer a phase change but not identify the specific phase entered by a material. While microscopic (atomic-level) diagnostic systems (e.g. DXRD) have been designed and implemented in Department of Energy's (DOE) National Laboratories complex, the unique nature of Sandia National Laboratories' Pulsed Power Facility (Z Machine) prohibits the use of such devices. The destructive nature of Z experiments presents a challenge to data capture and retrieval. Furthermore there are electromagnetic interference, X-ray background, and mechanical constraints to consider. Thus, a multi-part X-ray diagnostic for use on the Z Machine and Z-Beamlet Laser system has been designed and analyzed. Portions of this new DYnamic SCintillator Optic (DYSCO) have been built, tested and fielded. A data analysis software has been written. Finally, the radiance profile of the DYSCO's scintillator has been characterized through experiments performed at the University of Arizona.

ACKNOWLEDGMENT

The author would like to thank the scientists at the University of Arizona for assistance in the Radiance Characterization portion of this report, the team at the Z Machine and Z-Beamlet for making these experiments happen, and for the colleagues whose input helped tremendously.

CONTENTS

Nomenclature.....	11
1. Introduction	13
1.1. History of Field	13
1.2. Modern Day Examples	14
1.2.1. Omega Laser Facility: Laboratory for Laser Energetics	14
1.2.2. National Ignition Facility	15
1.2.3. Dynamic Compression Sector	15
1.2.4. Advanced Light Source.....	16
1.3. XRD on Z.....	16
1.3.1. History of XRD at Z and ZBL	17
1.3.2. Optical and Opto-mechanical Constraints.....	18
1.4. DISCO	18
1.4.1. Introduction	18
1.4.2. Optical Design Analysis	19
1.4.3. Optomechanical Design	20
1.4.4. Image Registration.....	21
1.4.5. Performance at ZBL/Chama	23
2. Theory	25
2.1. X-Ray Diffraction	25
2.2. Shock Compression Physics	26
2.3. Scintillator Physics	28
2.3.1. Fundamental Physics.....	28
2.3.2. Efficiency and Speed	29
2.4. Radiometry	29
2.4.1. Overview of Radiometric Nomenclature.....	30
2.4.2. Lambertian Radiators	31
2.4.3. Radiometry of optical lens systems	32
2.4.4. Radiometers	33
3. Methodology	35
3.1. Optical System with Fiber Relay	35
3.1.1. Updated Radiometry Requirements	35
3.1.2. Updated Optical Requirements	36
3.1.3. Updated Opto-Mechanical Constraints	37
3.2. Front-End Optical Design	37
3.2.1. Lens Design	37
3.2.2. Optical Parameters.....	38
3.2.3. Design Overview	39
3.2.4. Objective.....	39
3.2.5. Eyepiece	41
3.2.6. Combination.....	42

3.3.	Back-End Optical Design	42
3.3.1.	Optical Parameters	42
3.3.2.	Design Overview	43
3.3.3.	Objective	43
3.3.4.	Eyepiece	44
3.3.5.	Combination	46
3.4.	Radiometry	47
3.4.1.	Radiometry of Coupled Optical Relay Systems	47
3.4.2.	Front-End Radiometry	47
3.4.3.	Fiber Radiometry	47
3.4.4.	Back-End Radiometry	48
3.5.	Radiance Characterization Experiments	48
3.5.1.	Derivation of Gaussian Imaging Distances for The New Setup	50
3.5.2.	Setup	51
4.	Results and Analysis	53
4.1.	DYSCO Front-End Variants	53
4.1.1.	Optical Performance Metrics	54
4.1.2.	Tolerancing Analysis	59
4.2.	DYSCO Back-End	62
4.2.1.	Optical Performance Metrics	62
4.2.2.	Tolerancing Analysis	65
4.3.	Radiance Characterization	68
4.3.1.	Data Capture	68
4.3.2.	Data Analysis	69
5.	Conclusion	70
5.1.	Summary of Design Work	70
5.2.	Future Work	71
5.3.	Impact on Z Diagnostics	71
	References	73
	Appendix A. DISCO GUI User Manual	78
A.1.	The File Structure	78
A.2.	The Main App	78
A.3.	App Work-flow	78
A.3.1.	Prompt for overlay	78
A.3.2.	Load Pupil and Import Pupil sub-app	79
A.3.3.	Adjust ‘caxis’ and ‘pad’ button	79
A.3.4.	‘Trim’ and ‘Draw Circle’ Buttons	80
A.3.5.	Main App: Selecting, Rotating and Placing Pupils	82
A.3.6.	Selecting a Pupil	82
A.3.7.	Rotate Pupil	83
A.3.8.	Replace Pupil, Pupil Destination Panel, Alpha Modifiers Tab	84

A.3.9.	Notes on Manipulating Pupils	86
A.3.10.	Save Final Image Button	87
A.4.	Calibrating a Raw Image	87
A.4.1.	Inputs	88
A.4.2.	Purpose	88
A.4.3.	Steps	88

LIST OF FIGURES

Figure 1-1.	Dynamic Phase Change	14
Figure 1-2.	Z-DMP Load	17
Figure 1-3.	DISCO Schematic	19
Figure 1-4.	DISCO Layout	19
Figure 1-5.	DISCO Components	20
Figure 1-6.	DISCO Optomechanics	21
Figure 1-7.	DISCO GUI Process	21
Figure 1-8.	DISCO GUI Flowchart	22
Figure 1-9.	DISCO XRD Data	23
Figure 1-10.	DISCO XRD Data	24
Figure 1-11.	DISCO XRD Data	24
Figure 2-1.	Single Crystal vs Poly-Crystal XRD	26
Figure 2-2.	Aluminum p-t Diagram	27
Figure 2-3.	Iron p-t Diagram	28
Figure 2-4.	Radiometric Transfer	30
Figure 2-5.	Lambertian Cosine Law	31
Figure 2-6.	Lambertian Cosine Law	32
Figure 2-7.	Radiometric Throughput	33
Figure 2-8.	Basic Radiometer	34
Figure 3-1.	Starting Point Layout	40
Figure 3-2.	Fold Mirror Inserted Layout	40
Figure 3-3.	Eyepiece Starting Point	41
Figure 3-4.	Eyepiece	41
Figure 3-5.	Combination	42
Figure 3-6.	Double Gauss Starting Point Layout	44
Figure 3-7.	Telecentric Double Gauss Layout	45
Figure 3-8.	Cooke Triplet Starting Point Layout	45
Figure 3-9.	Telecentric Cooke Triplet Layout	46
Figure 3-10.	Combination Layout	46
Figure 3-11.	Fiber Attenuation	48
Figure 3-12.	Scintillator	49
Figure 3-13.	Radiometer Geometry	50
Figure 3-14.	FLIR Camera	52
Figure 3-15.	Radiance Characterization Setup	52
Figure 3-16.	Radiance Characterization Setup	53

Figure 4-1.	DYSCO in Containment	54
Figure 4-2.	DYSCO-L Layout	54
Figure 4-3.	DYSCO-Straight Layout.....	55
Figure 4-4.	DYSCO L Optomechanics	55
Figure 4-5.	DYSCO Straight Optomechanics.....	56
Figure 4-6.	Front End Spot Diagram.....	56
Figure 4-7.	Front End Wavefront Error	57
Figure 4-8.	Front End MTF Resolution	58
Figure 4-9.	Front End Image Simulation	59
Figure 4-10.	Front End Lab Capture	59
Figure 4-11.	Front End Histogram.....	61
Figure 4-12.	Front End Yield	62
Figure 4-13.	Layout.....	63
Figure 4-14.	Back End Spot Diagram	63
Figure 4-15.	Wavefront Error	64
Figure 4-16.	MTF Resolution	65
Figure 4-17.	Back End Histogram	67
Figure 4-18.	Back End Yield	68
Figure 4-19.	Radiance Data	69
Figure 4-20.	Radiance Data	69
Figure 4-21.	Light- Taper Coupling	70
Figure A-1.	Import Pupil App	79
Figure A-2.	Padding Image	80
Figure A-3.	Trace Pupils	81
Figure A-4.	Trace Pupils Completed	81
Figure A-5.	Pupils in GUI	82
Figure A-6.	Select Pupil	83
Figure A-7.	Rotate Pupil	84
Figure A-8.	Alpha Modifiers.....	84
Figure A-9.	Placing Pupil	85
Figure A-10.	Maneuver Pupil	85
Figure A-11.	Pupil Overlap	86
Figure A-12.	Final Pupil Placement	87

LIST OF TABLES

Table 2-1.	Radiometric Nomenclature	31
Table 3-1.	Compliance Matrix of the DYSCO Front End	39
Table 3-2.	Compliance Matrix of the DYSCO Back End.....	43
Table 4-1.	Tolerance Parameters for the DYSCO Front-End	60
Table 4-2.	Tolerance Parameters for the DYSCO Back End	66

NOMENCLATURE

A-K anode-cathode

APS Advanced Photon Source

BCC body centered cubic

CCD charge-coupled device

DAC diamond anvil cell

dB decibel

DCS Dynamic Compression Sector

DISCO DIffraction SCintillator Optic

DMP Dynamic Material Properties

DOE Department of Energy

DXRD dynamic X-ray diffraction

DYSCO DYnamic SCintillator Optic

EMP electromagnetic pulse

EOS equation of state

EPD entrance pupil diameter

f focal length

Fe iron

FOV field of view

FWHM full width at half maximum

GUI graphical user interface

HCP hexagonal close packed

He helium

HOPG highly oriented pyrolytic graphite

ICF inertial confinement fusion

keV kiloelectronvolt

LLE Laboratory for Laser Energetics

LSO:Ce lutetium oxyorthosilicate, cerium doped

m magnification

MeV megaelectronvolt

Mn manganese

MTF modulation transfer function

n moles of gas

NA numerical aperture

NIF National Ignition Facility

ns nanosecond

OPD optical path difference

P pressure

P43 $Gd_2O_2S : Tb$

P47 $Y_2SiO_5 : Ce, Tb$

PDV Photonic Doppler Velocimetry

ps picosecond

PIMAX-4 Princeton Instruments fast-gated intensified camera

PMMA poly(methyl methacrylate)

POF plastic optical fiber

PXRDIP Powder X-Ray Diffraction Image Plate

R gas constant

RES Radiation Effects Sciences

SCDI Spherical Crystal Diffraction Imager

T temperature

TARDIS TARget Diffraction In Situ

TIR total internal reflectance

USP United States patent

V volume

VISAR Velocimetry Interferometer System for Any Reflector

XRD X-ray diffraction

Z Z-Machine

ZBL Z-Beamlet

Zr zirconium

1. INTRODUCTION

1.1. History of Field

X-ray diffraction (XRD) is a powerful tool to interrogate a solid material's crystalline structure. X-rays are used because their wavelengths are on the order of the material's lattice parameter (spacing between atoms). Thus, the fundamental phenomenon of diffraction is achieved when the X-ray source wavelength, angle of incidence, and spacing between atoms (lattice parameter) satisfy Bragg's Law:

$$2d \sin \theta = m\lambda \quad (1)$$

By measuring the ray angles of incidence and exitance, the spacing between atoms may be determined and thus, the structure can be deduced.

After Wilhelm Roentgen discovered X-rays, scientists wanted to show that X-rays were indeed part of the electromagnetic spectrum by proving X-rays would behave like waves. Initial work began with Max Von Laue, who showed that a crystal will act as a diffraction grating and diffract X-rays thus validating the wave nature of X-rays [1]. The father-son duo of William Henry Bragg and William Lawrence Bragg, derived the governing formula for diffraction (Equation 1)[2]. Finally, Peter Debye and Paul Scherrer expanded Laue's work to include powder crystal diffraction by measuring diffraction lines originating from X-ray illuminated lithium fluoride powder [3].

One important application of XRD is the study of materials under high pressure compression. Static high pressure work in the early 20th century was dominated by the use of the so-called Bridgman anvil and piston-cylinder device that enabled interrogation of materials up to 100 kbar (= 10 GPa) [4]. Next, Drickamer and his co-workers improved the devices and extended their pressure range to several hundred kbars to discover new phenomena of solids at high pressure [5]. Later, the diamond anvil cell (DAC) was developed in which a material sample on the order of a few millimeters was squeezed between small ends of two classically-cut diamonds. By applying pressure to the large ends of the diamonds, pressure on the sample was multiplied, and certain DAC configurations have reached pressures up to 1-2 Mbar [6]. In addition, the diamonds are optically and X-ray transparent, so they double as windows to the interrogating radiation [7]. The diffraction pattern from the 'ambient' (uncompressed) material differs from its compressed pattern as the compression induces a change in its atomic structure causing the XRD lines to shift or new ones to appear.

Later, static XRD evolved to the interrogation of crystal structures under dynamic stress or compression. So called Dynamic X-ray Diffraction (DXRD) work involves the impulse of material via shock or ramp waves (shock or ramp compression). These may be induced by laser deposition [8], explosives detonation, or metal flyer impact[9]. The induced shock changes the crystal structure and this change is captured by different X-ray sensitive media. In addition, DXRD allows compression of samples to reach the TPa regime [10].

To make a distinction, static XRD is the compression of a sample to an arbitrary high pressure first and an XRD measurement second. Conversely, DXRD is the measurement of a compressed

sample's phase while the material is under shock or ramp compression. Also, DXRD allows higher pressures to be reached over larger area samples. Finally, DXRD also requires measurements with nanosecond time scale resolution. For reference in Figure 1-1, the intended XRD measurement would be the new phase after the 1D elastic and 3D plastic solid phases had passed.

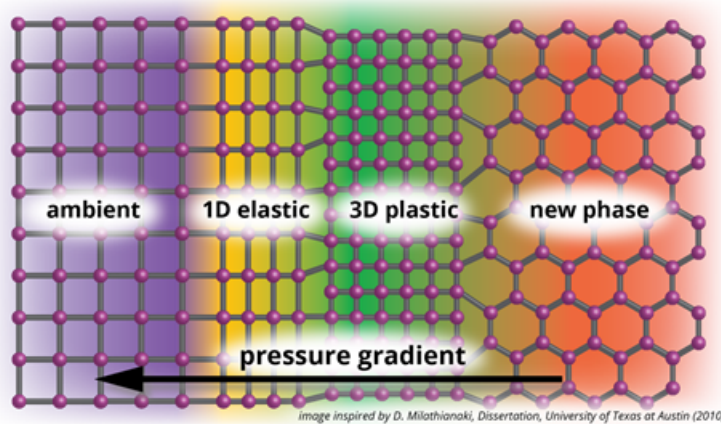


Figure 1-1 Phases a material may enter while under shock or ramp loading conditions.

For example, in order to explore fundamental geophysics, pioneering DXRD work by Kalantar and colleagues observed diffraction lines from compressed iron at three distinct times- which showed the iron α - ϵ phase transformation ‘in real time’. The variation of the lines directly informed the change of phase from BCC (Body Centered Cubic) to HCP (Hexagonal Close Packed) [11].

Later, a shocked compressed iron sample was observed going from the ambient BCC phase to the HCP phase at 170 GPa. This result was informative as the pressures interrogated approximated the Earth’s core conditions [12].

1.2. Modern Day Examples

Modern day X-ray diffraction testbeds are broad in scope with many examples across the Department of Energy’s (DOE) National Laboratories. These sister organizations have the capability to perform XRD work in their synchrotron, gas gun, pulsed power, and high-powered laser systems.

1.2.1. *Omega Laser Facility: Laboratory for Laser Energetics*

The Laboratory for Laser Energetics (LLE) is a research facility that is part of the University of Rochester in Brighton, New York. The Omega laser system within the LLE facility contains 60 laser beams that focus 30 kJ of energy onto small targets (1 mm diameter). The LLE facility’s

Powder X-ray Diffraction Image Plate (PXRDIP) diagnostic is a simple approach for powder diffraction. A thin sample of interest is irradiated by a series of drive lasers that compress the sample to a uniform pressure for a set period of time. A second series of lasers illuminate a metal foil target that emits X-rays which are collimated by a pinhole. The sample, held between two diamond plates, is illuminated in the front by the collimated X-rays and interrogated by the back via a velocimetry diagnostic, such as VISAR (Velocimetry Interferometer System for Any Reflector) [13]. The 2θ transmitted diffraction signal is captured by X-ray sensitive image plates suspended inside a rectangular housing. X-ray diffraction patterns can be captured just under the terapascal regime [14].

1.2.2. *National Ignition Facility*

The National Ignition Facility (NIF) is the largest laser in the world. Located in the California Bay Area at Lawrence Livermore National Laboratory, this facility dwarfs the Omega laser system as it houses 192 laser beams that can focus up to 2 MJ of energy onto small targets. This equates to higher achievable pressures and temperatures. At the NIF testbed, the TARDIS (TARrget Diffraction In Situ) diagnostic uses ramp loading up to 5 TPa and also uses image plates to capture XRD data [15]. The target holder is the similar to the Omega setup: a sandwich assembly contains a sample and a glass window with the optional addition of a heatshield and ablator material for uniform compression of the actual sample. Also, VISAR is employed to characterize the assembly velocity which determines the pressure history.

1.2.3. *Dynamic Compression Sector*

Another testbed is the XRD detector at the Dynamic Compression Sector (DCS) of the Advanced Photon Source (APS) at Argonne National Laboratory. APS is a synchrotron that accelerates electrons to 450 MeVs, then boosted to 7 GeV and sent through the electron storage ring. Here, electrons can be diverted into straight sections that produce X-ray radiation [16]. The XRD detector at DCS has time gating capability via dynamic shutters in the ‘front-end’ and camera-equipped time gating on the ‘back-end’. The front-end coupling has a phosphor-coated fiber optic plate that is attached to a fiber taper which in turn is attached to a micro channel plate image intensifier. This back-end is repeated across four cameras, each gated to a separate time window in the experiment’s lifetime.

This system looks at four distinct X-ray bursts at energies above 7 keV with options for different phosphor thicknesses. The mechanical shutter on the front end protects the system from X-ray saturation, while the back-end time gating is to look at the respective X-ray burst, noting the decay time of the scintillators used (LSO:Ce on the front end, P47 intensifier in the camera). For example, DXRD of copper targets were performed using gas-gun flyer impactors and interrogated with 23 keV X-rays. Researchers saw XRD of copper in its ambient and compressed states, and then its state after it was released from a sapphire backing window [17].

1.2.4. Advanced Light Source

Perhaps the closest system to the work presented in this thesis is the Blue-1 diagnostic and its predecessor, the Noir-1. The purpose of the Blue-1 diagnostic was to interrogate crystallized biological materials. Originally developed at Argonne National laboratory, the system uses a lens coupling front-end that couples the emittance of an X-ray sensitive, phosphor-coated mylar sheet to a CCD detector. This nine-element lens coupling system can effectively image a 100-micron diameter spot [18]. Currently it is being used for sampling of crystallized biological material at the Advanced Light Source synchrotron at Lawrence Berkeley National Laboratory.

Our system presented in this thesis, referred to as the DIffraction SCintillator Optic (DISCO), conceptually borrows from all these systems in that it is a time gated, lens coupled system, which could also fit inside a containment hardware system to look at targets under shock and ramp loading conditions within a pulsed power facility. For example, the DISCO diagnostic uses a lens coupling system due to simplicity of design, as opposed to DCS's fiber plate-fiber taper-micro channel plate construction. However, the pulsed power experimental environment also prohibits the use of image intensifiers, as found in the DCS setup.

1.3. XRD on Z

Sandia National Laboratories' Z Pulsed Power Facility (known as the 'Z Machine') is the largest pulsed power facility in the world and is capable of recreating pressure and temperature environments that approximate the center of planets and stars. It does so by storing electrical charge in capacitor banks and synchronously discharging the electrical energy in a controlled pulse shape on the order of nanoseconds [19]. The Z Machine is capable of many types of experiments including Inertial Confinement Fusion (ICF), Dynamic Material Properties (DMP), and Radiation Effects Science (RES). X-ray diffraction primarily serves the DMP style experiments as a way to interrogate material phase states during different loading conditions.

The Z-DMP coaxial load, as shown in Figure 1-2 is used for shock compression experiments on Z. The load is comprised of two anode flyer plates that sandwich a central cathode stalk. This forms two anode-cathode (A-K) vacuum gaps that can be short circuited with a shorting cap to provide current flow. Once current flows through the anode plate and the cathode stalk, a magnetic field is created within the vacuum gaps. The cross product of the surface current and the magnetic field produces a stress wave that launches the anode flyer plates onto the samples.

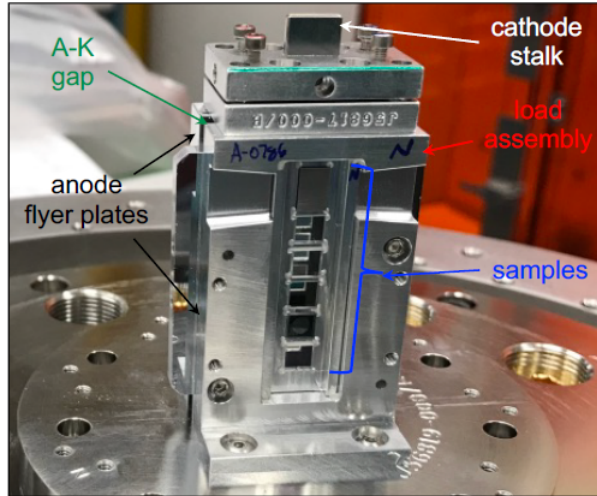


Figure 1-2 The Z-DMP coaxial load [20].

VISAR and Photonic Doppler Velocimetry (PDV) diagnostics have been used to infer phase changes of materials under investigation. Unfortunately, VISAR and PDV only notify the change of a phase without identifying the specific initial and final phases. Thus, the development of X-ray diffraction diagnostics has been a high priority for the Z Machine and its complementary facility, Z-Beamlet Laser (ZBL) system.

As shown in the previous section, different XRD diagnostics at various testbeds have been deployed to identify the phases in which the materials are transitioning. However, Z has several unique experimental challenges that preclude using the XRD schemes that have worked at other dynamic compression facilities. First, the large current and magnetic fields of Z generate a tremendous amount of high energy photons, including MeV-scale photons near the load, which results in a very high x-ray background. Second, very strong electromagnetic pulses (EMP) are emitted when Z fires, which could damage electronics within close range of the load or at the very least produce unwanted early triggers. Third, the Z environment is very destructive in which large amounts of debris scattered throughout the load region, so direct x-ray detection and subsequent data retrieval would be quite infeasible.

Thus, a useful diagnostic system would be one that is time gated, such that the researcher can specify the time window in which to observe some X-ray interaction without the background X-ray radiation from the Z Machine itself obscuring the measurement. The diagnostic system would have to fit inside an enclosure created for containing Z shot debris. Finally, the diagnostic system should be modular as to allow a portion of the diagnostic to be consumed upon every Z shot.

1.3.1. History of XRD at Z and ZBL

Previously, a simple XRD diagnostic, referred as the Spherical Crystal Diffraction Imager (SCDI), was developed for Z-XRD experiments. Briefly, the SCDI diagnostic utilizes the ZBL

laser to generate 6.2-keV Mn-He α x-rays to probe a shock-compressed sample on the Z-DMP load. The SCDI diagnostic relied on a spherical crystal that reflected 6.2 keV X-rays into a tungsten box that was lined with X-ray sensitive image plates. [21] Image plates have an infinite integration time and cannot be time gated. Therefore, the time history of the XRD event is missing. Another key deficiency of the SCDI was its inability to successfully image high energy X-ray radiation ($> 10\text{keV}$). Furthermore, the highly oriented pyrolytic graphite (HOPG) crystal itself relies on diffraction to ‘reflect’ the beam of interest, which drastically reduced the signal. Ultimately, SCDI is incompatible with Z-Containment experiments because the XRD data recorded on the image plates cannot be retrieved from the Z-Containment vessels. [20].

1.3.2. *Optical and Opto-mechanical Constraints*

Thus, the DISCO diagnostic and its second-generation variant, DYSCO (DYnamic Scintillator Optic), are needed to fulfill the following requirements.

Optically, DISCO/DYSCO needs to convert X-ray radiation into visible light via a scintillator. There needs to be a modular front-end lens coupler that collects the scintillation radiation and images onto an imaging fiber optic cable. This optical fiber bundle would transport the data out of Z’s harsh environment. The final modular portion would be the back-end lens coupler that couples light from the fiber to the camera sensor. The camera sensor shall be an intensified CCD camera that has time-gating capability of around 100 ns to temporally filter out Z’s background X-ray noise.

Optomechanically, the front-end shall be housed inside a tungsten cylindrical tube that shields the diagnostic from stray X-ray radiation. The entrance face of the diagnostic should be shrouded with a conical tungsten nose cone that matches the diffracted X-rays’ angular rays of 30°. The lens holders and spacers should be aluminum as that is a relatively inexpensive material to machine. The object to image distance should be small enough to fit inside the walls of the containment device.

Mechanically, the Z Containment vessel is only 8 inches in diameter, so the diagnostic front-end must accommodate the Z-DMP load hardware stalk as well as route the fiber bundle through the top of the containment device. Additionally, the front face of the DISCO should be roughly 45 mm away from the DMP sample to achieve the desired scintillator full field of view of 30° that captures the XRD data .

1.4. *DISCO*

1.4.1. *Introduction*

The DISCO diagnostic was born out of a need to measure dynamically compressed targets in Z and ZBL experiments (‘shots’) while accommodating unique spatial constraints at Z . The aim is to have a time gated, modular system that will ultimately fit in the Z Containment hardware configuration. The first iteration was designed by Sandia scientist Marius Schollmeier, previously

of ORG 01682. It contains front- and back- end lens coupling sections that sandwich a multi-core fiber bundle relay. As discussed in Section 1.2, this system borrowed from several different diagnostic systems in that it is a time gated, modular systems that is containment compatible, while have sacrificial pieces that cannot survive a Z experiment.

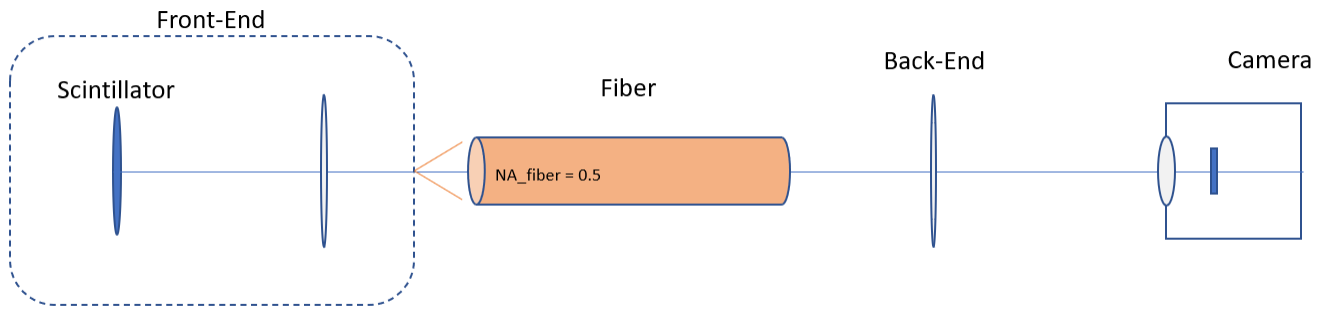


Figure 1-3 DISCO Schematic.

1.4.2. *Optical Design Analysis*

The DISCO front end is a seven-element system with a focal length of 25.5 mm working at $F/1$. While not directly containment compatible, it proved the efficacy of a lens-coupled scintillator module that could capture signal well away from the camera sensor.

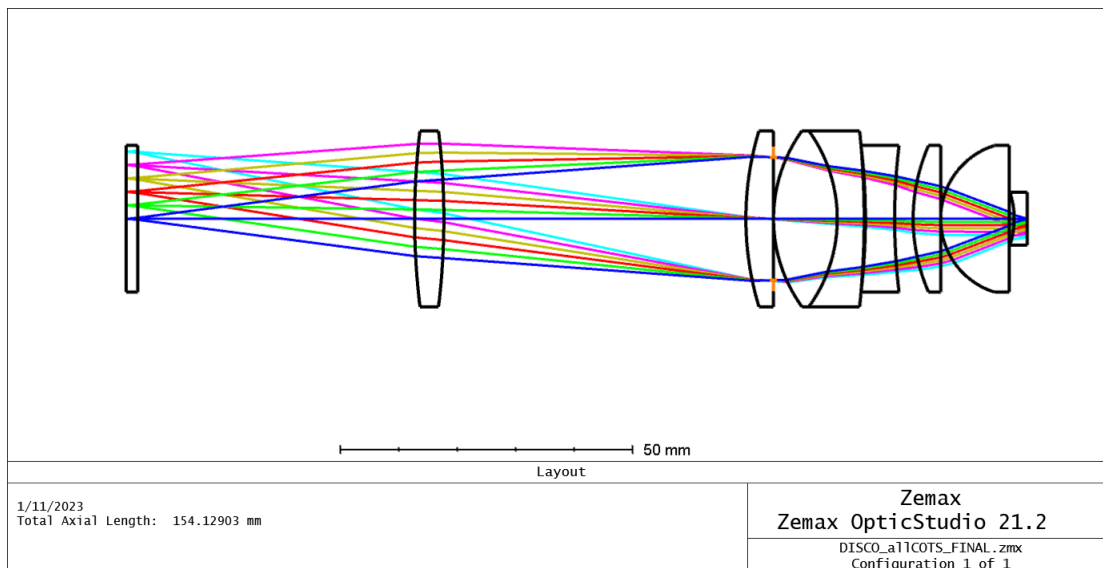


Figure 1-4 DISCO Layout consisting of seven lens elements. The first element is the glass substrate for the scintillator material. All lenses are COTS (commercial off the shelf) components.

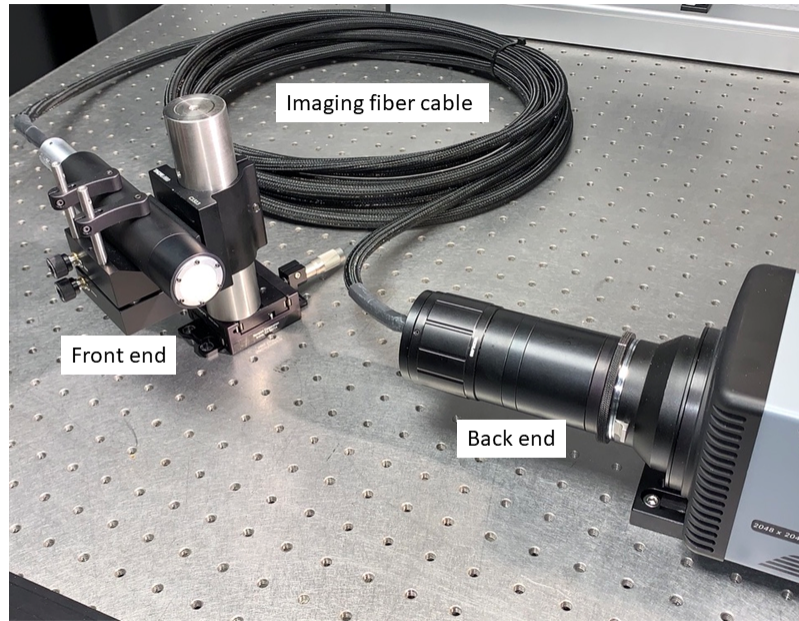


Figure 1-5 DISCO Components. The three-part DISCO allows the front-end to be placed away from the camera sensor.

A key feature of the DISCO system is the ‘imaging fiber-cable relay’ (originally sourced from the vendor FiberFin). The imaging fiber-cable holds a hexagonally-arranged super-bundle of seven imaging fiber bundle ‘pupils’ referred to as the ‘rosette’, which is about 6-mm in diameter. Each fiber bundle (e.g. Asahi Kasei Multicore POF MBL-2000-24) has a numerical aperture of 0.5 and is 2-mm in diameter that is comprised of 13,000 individual high spatial resolution (15-micron diameter) PMMA plastic core fibers.

The DISCO back-end was originally designed for a larger sensor. Thus, the back-end image would overfill the PIMAX4 camera’s 1024i sensor when using the same back-end. As a stopgap solution, two 10x microscope objectives were placed together to form an imaging system. This imperfect solution under-filled the sensor but allowed ‘uncropped’ data capture. The system required a resolution of 20-line pairs per mm to resolve the alignment target features.

1.4.3. Optomechanical Design

The lenses were held by Thorlabs Lens tubes, retaining rings, custom spacers and custom ‘poker chips’.

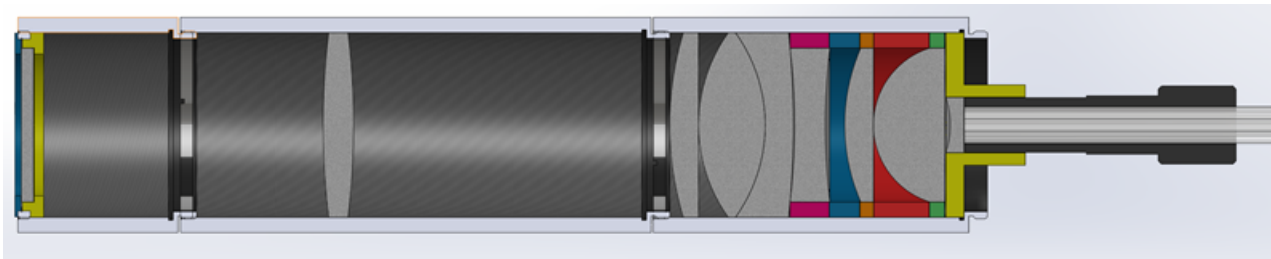


Figure 1-6 DISCO Optomechanics. The DISCO Lens holders are comprised of Thorlabs lens tubes and custom spacers and ‘poker chips’ (radial lens holders).

1.4.4. *Image Registration*

The fiber bundle geometry did not conserve the spatial location nor the rotational orientation of each pupil in the rosette. Therefore, an image processing software was developed by the author to correctly register the pupils to their correct orientation and position.

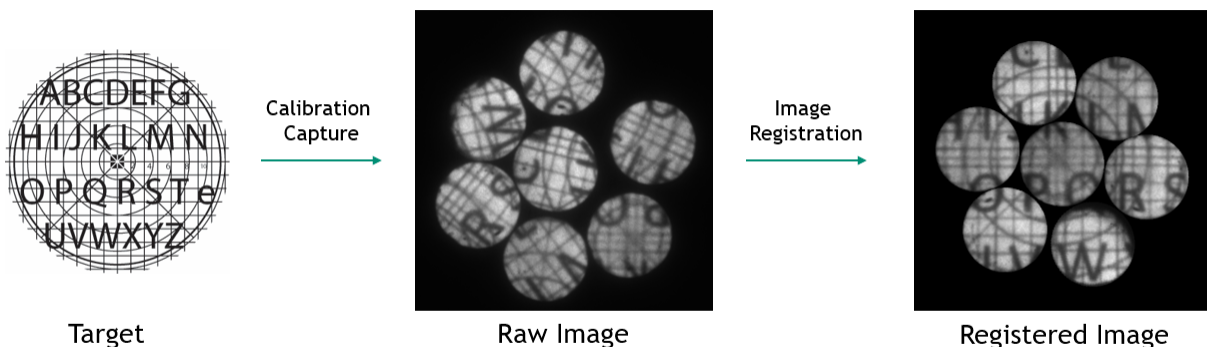


Figure 1-7 DISCO GUI Process. Calibration steps

This image processing Graphical User Interface (GUI) was developed in MATLAB’s App Designer suite and consists of the main GUI and one sub-GUI, many subroutines, and internal functions. The main workflow is shown in Figure 1-8 and described below. A more detailed explanation can be found in Appendix A. The GUI will import a reticle image and export a ‘pupil bank’ mat file and a tiff image. The pupil bank is a vector of ‘pupil’ objects whose fields include the pupil’s unique identifier index, the original center and radius, the translation and rotation of the pupil, and the actual image of the pupil and its binary mask.

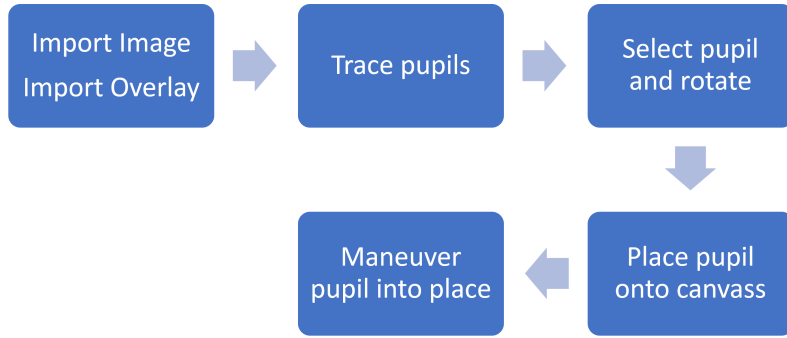


Figure 1-8 DISCO GUI Flowchart. Calibration steps

1. Import Image and Overlay

- a) Import a tiff file that holds the reticle raw image. This is a 1024x1024 image.
- b) Adjust contrast of reticle.
- c) Pad the image to a 2048x2048 size.

2. Trace Pupils

- a) Circumscribe a circle object onto a pupil and thus save the pupil location and radius.
- b) Iterate over all seven pupils.

3. Select Pupil and Rotate

- a) From a dropdown menu, select a pupil and rotate it such that it is upright, using the grid lines as help.
- b) ‘Lock’ the rotation to save the rotation value .

4. Place Pupil onto Canvass

- a) Select a destination pupil to transplant current pupil.
- b) Click ‘Replace’.

5. Maneuver Pupil into Place

- a) Using the W, A, S, and D keys, or by clicking the buttons, maneuver the pupil until it overlaps with the corresponding area of the overlay image.

1.4.5. Performance at ZBL/Chama

The Z Backlighter facility that houses the large ZBL system, and the smaller Chaco laser has a selection of target chambers where experiments are fielded. One such target chamber, the Chama target chamber, is where ambient and laser-shocked XRD experiments are conducted, among others. The DISCO diagnostic was fielded at Chama to prove the efficacy of capturing a shocked XRD data. Results are discussed in [20] and briefly reviewed here.

Two experiments were conducted to show the efficacy of the DISCO diagnostic. In the first experiment, ambient XRD data was obtained when an uncompressed zirconium (Zr) sample, which has HCP structure, was probed by 6.7 keV X-rays generated by an iron (Fe) foil target ZBL. First, a circular image plate (25-mm diameter) was initially placed at the DISCO front-end's scintillator location of 40 mm from the Zr sample. Figure 1-9(a) shows the XRD data measured by the image plate. The corresponding XRD angular line profile showed the single XRD peak (102) at 58.6° has a full-width-half-max (FWHM) of 1.3° , while the 2 close XRD peaks (002) and (101) at 42.2° and 44.25° were well resolved (see Figure 1-9(b)).

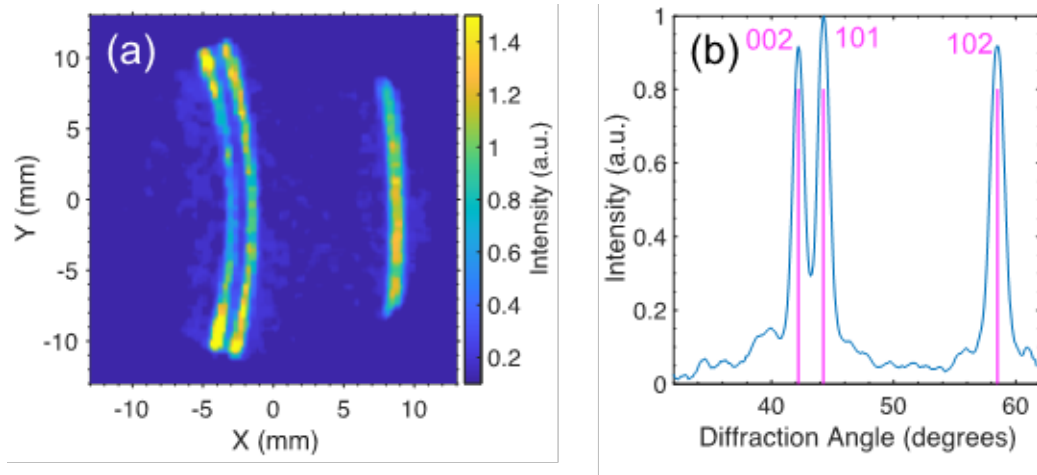


Figure 1-9 (a) Experimental ambient XRD data measured by imageplate at DISCO front-end's scintillator. **(b)** XRD angular line profile and simulation of diffraction peaks.

Next, the image plate was removed and the XRD measurement was repeated with the DISCO using a P43 phosphor, as shown in Figure 1.10. The 7 pupils of the imaging-fiber-cable were clearly observed as the XRD rings traverse them and the in-between null spaces (see Figure 1-10(a)). The XRD angular line profile of Figure 1-10(b) showed the single XRD line (102) at 58.6° had a slightly wider FWHM of 1.5° compared to the image plate at the DISCO front-end measurement. Although the 2 close XRD lines (002) and (101) at 42.2° and 44.25° were slightly more convolved, they were still sufficiently resolved by the DISCO diagnostic.

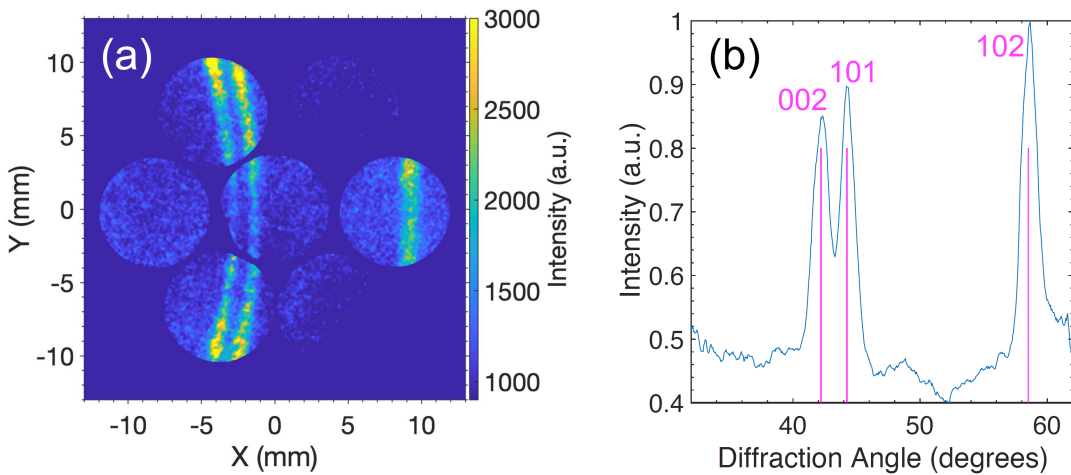


Figure 1-10 (a) Experimental ambient XRD data measured by DISCO with a P43 scintillator. **(b)** XRD angular line profile and simulation of diffraction peaks.

In the second experiment, the aim of the experiment was to capture dynamic XRD rings from a shock compressed Zr sample that was probed by X-rays as produced by 6.7 keV X-rays produced from an Fe target irradiated by ZBL. At an adjacent time, the Chaco laser would compress the Zr XRD sample such that compressed XRD rings would be produced. Figure 1-11(a) shows the dynamic XRD data measured by DISCO, which has noticeable changes in the texture of XRD rings. Figure 1-11(b) shows the XRD angular line profile of the HCP (002), (101), and (102) peaks have shifted to 42.5° , 44.6° , and 59.1° , respectively. The respective individual shifts of 0.3° , 0.35° , and 0.5° correspond the shocked Zr sample having a reduction in its HCP lattice spacing of $\delta d/d = 0.74\%$ or a compression of $\rho/\rho_0 = 1.022$.

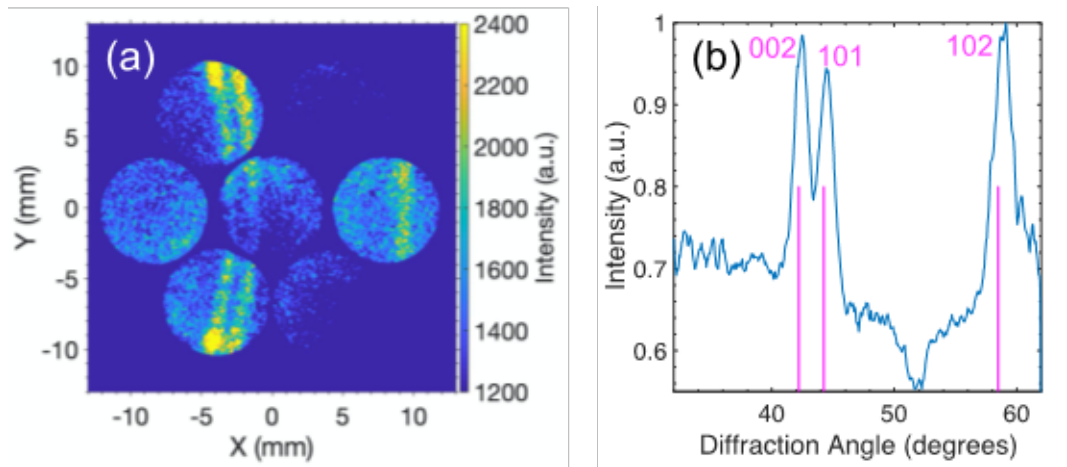


Figure 1-11 (a) Experimental ambient XRD data measured by DISCO with a P43 scintillator. **(b)** XRD angular line profile and simulation of diffraction peaks.

2. THEORY

2.1. X-Ray Diffraction

X-ray diffraction arises due to X-rays interacting with a material, so an understanding of basic material properties is in order. Solids that are not amorphous will have a periodic structure of atoms arranged in a lattice. These atoms may have a “seed” arrangement in which a sequence of atoms is repeated across one, two, or three dimensions. This is referred to as the unit cell, which is then repeated to form a crystal.

The unit cell is defined by three vectors: $(\mathbf{a}, \mathbf{b}, \mathbf{c})$. Any point in 3D space is defined by the vector:

$$\mathbf{q} = u\mathbf{a} + v\mathbf{b} + w\mathbf{c} \quad (2)$$

with the origin at $u = v = w = 0$. The unit cell is also described by the three angles between the vector directions, namely, α, β, γ and their lengths a, b, c all referred to as the lattice parameters.

The ideal crystal structure, one with no discontinuity, will define lattice points coincident with the atoms or molecules that form the crystal. These lattice points are parallel to each other and equi-spaced and form lattice planes. The spacing between the planes is called the “d-spacing”. Another construct called Miller indices (h, k, l) describe a family of crystallographic planes by dividing the unit cell edges into (h, k, l) equal parts. Should the Miller index be zero, the intersection is thought to be at infinity and therefore describes a plane parallel to h, k , or l .

This ‘real’ description of lattices and can be expressed by the thought construct of a reciprocal lattice. Where a coordinate system is described by vectors $\mathbf{a}^*, \mathbf{b}^*, \mathbf{c}^*$ and are in the same direction as $\mathbf{a}, \mathbf{b}, \mathbf{c}$ with reciprocal lengths $1/a, 1/b, 1/c$. The points on the coordinate system correspond to a family of planes in the ‘real’ lattice. For example, the point $(1,0,0)$ in reciprocal space refers to the $(1, 0, 0)$ family of planes.

The reciprocal lattice definition can be used to then describe diffraction from elastically scattered waves of a single crystal. Because elastic scattering yields an exitant wave vector whose length is equal to the incoming wavevector (\mathbf{k}_0), a sphere may be drawn with the radius being the length of the wavevector: $1/\lambda$. This sphere is referred to as Ewald’s sphere. Superimposing the incoming and exiting vector onto the reciprocal lattice 3D “grid” will indicate the presence of diffraction peaks if and only if a point (family of planes) on the reciprocal lattice space coincides with the surface of the Ewald Sphere. The vector originating on the origin of the Ewald sphere and ending on the intersection lattice point is then \mathbf{k}_1 , the exitant wavevector. The result is a diffraction point in 3D space.

The description of poly-crystal diffraction may be expanded to diffraction from an infinite number of tiny crystals (“crystallites”). As before, a monochromatic beam irradiates a collection of crystallites. Each crystallite has a random orientation and thus, has also a random orientation of its reciprocal lattice. The result is a uniform ring of lattice point-Ewald sphere interceptions. The ring is referred to as a “Debye-Scherrer Cone” and several cones may exist for multiple reciprocal lattice points based on the wavelength used. [22]

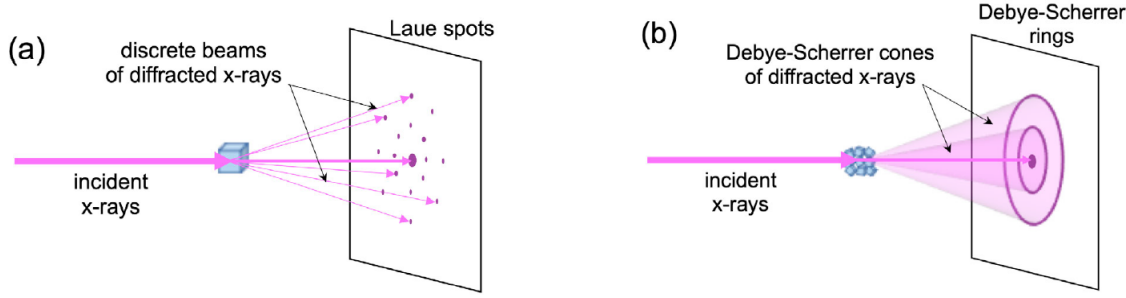


Figure 2-1 Single Crystal vs Poly-Crystal XRD. (a) A single crystal diffraction pattern will show discrete peaks or “Laue spots”. (b) A polycrystalline sample will effectively rotate the peaks about the axis to form “Debye Scherrer rings”. This result is due to the random orientation of each crystallite forming a discrete peak in its frame of reference [23].

2.2. Shock Compression Physics

Shock compression physics requires the fundamental knowledge of thermodynamics, which is the study of how temperature and other energy modes relate to material properties. [24] In thermodynamics, the *state* is the description of a material at a given temperature, pressure, and volume. An equation of state may be a closed form solution that describes the material at any given value of variables constituting the *state*. For example, such a closed form solution may be the ideal gas law:

$$pV = nRT \quad (3)$$

where p is pressure, V is volume, n is the number of moles of gas, R is the gas constant, and T is the absolute temperature.

When a closed form solution does not exist (i.e., most of the time), a P-T phase diagram is used. A P-T diagram charts the phase of material (solid, liquid or gas) for a given pressure and temperature (see Figure 2-2). It also denotes the location where phase transitions may occur along lines of phase equilibrium. The locations of phase transitions are experimentally calculated, and this is referred to as a material’s equation of state (EOS). To transition phases, either the temperature or pressure changes (increases) for a certain volume of material. Transitions can be forced by sudden increases in pressure as found in the strategy of shock compression. A change of phase is, in essence, a change in atomic or molecular structure of solid material before the material transitions into a new solid phase, liquid, or directly to gas.

Shock compression represents the response of a material along its principal Hugoniot, i.e. the states produced by passage of a steady, single shock wave produced from ambient conditions, which produce higher temperature states at a given compression. In addition to Hugoniot curves for EOS measurements, two other classes of curves of interest are the compression isotherms and isentropes. The isentrope generally lies in-between the isotherm and Hugoniot curves, is second order tangent to the Hugoniot at the common starting state, and represents a reversible loading process. Whereas a shock experiment generally yields only the single final P-V point on the

Hugoniot; an isentropic experiment yields a continuum of points along the isentropic loading path.

There are various techniques to impulse a material to change phase. In a controlled lab setting, this is done by sending an as-nearly 1-D plane pressure wave into a material. Pressure can be exerted via an explosive or a gas gun that drives a flyer plate onto a material. The Z Machine magnetically drives a flyer plate onto a material sample as in the case of DMP style ‘shots’ [25].

Alternatively, pressure fronts can also be created via laser energy deposition that ablates a material sending a shock wave that is as large as the beam diameter into a sample target [26]. In any case the 1-D plane wave hits the material thereby “shocking” it and changing the molecular structure.

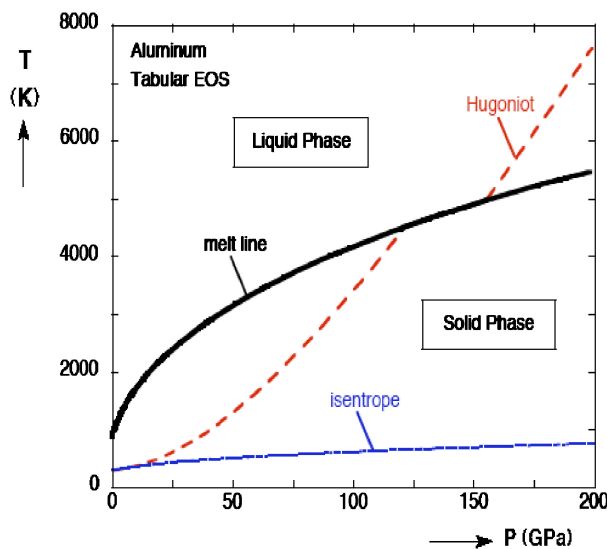


Figure 2-2 The pressure-temperature phase diagram of Aluminum [26].

Note that there are many phases in the solid ‘state’ of materials. For example, iron has a solid phase (see Figure 2-3) which corresponds to body centered cubic (BCC) or hexagonal close packing (HCP) arrangement of atoms for a given volume when at ambient conditions (former) and higher pressure and temperature (say 11 GPa and 700 K in the latter) [27]. Why is this important? Well, diagnostic devices that leverage x ray diffraction typically measure solid-to-solid phase transitions due to signal amplitude considerations.

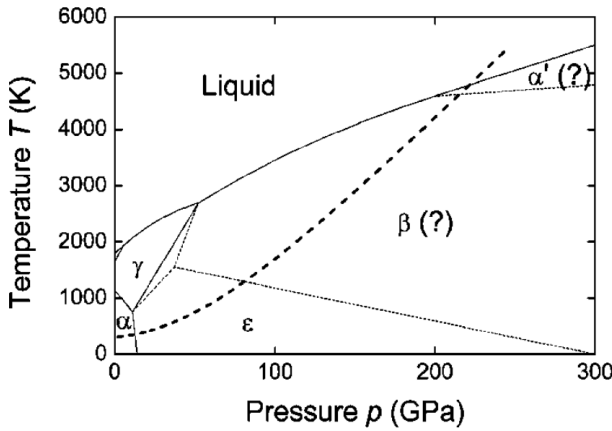


Figure 2-3 The phase-temperature diagram of Iron. The dotted line represents the Hugoniot and the α (BCC) to ϵ (HCP) phase transition is shown [28].

2.3. Scintillator Physics

2.3.1. Fundamental Physics

Radiation-material interactions differ based on the type of material used. All materials absorb reflect and/or transmit incoming radiation to some degree but some materials can absorb radiation and re-emit new radiation. This is what is known as fluorescence, phosphorescence, and scintillation. All three are based on incoming radiation interacting with the atomic structure of material and emitting some new kind of radiation. This occurs in three stages: *Conversion*, *Transport*, and *Luminescence*[29].

First, conversion involves the processes of the photo electric effect and Compton scattering[29]. The photoelectric effect is the emission of charged particles from a material when electromagnetic radiation is incident upon it. The total energy of the radiation is transferred to an electron inside the material. The photoelectric effect differs from Compton scattering in that it completely transfers all energy to an electron rather than a partial energy transfer that is defined with Compton scattering. The Compton effect also is valid for higher energy photons. Compton scatter can be understood as a photon-matter interaction where the mass-less photon collides with an atom's loosely held (outer shell) electron. This collision yields the scatter of the photon and the electron, described as the recoil electron, which creates secondary ionization [30].

Next, transport is the process where electrons and hole pairs travel through the material. This process is subject to several delays, losses, or signal degradation such as nonradiative recombination or manufacturing defects.

Finally, there is luminescence which is the stage where the electron hole pairs reconstitute and emit radiation [29].

2.3.2. Efficiency and Speed

Scintillators would ideally convert all high energy (X-ray or γ -ray) radiation into visible light instantly. However, the two main drivers against scintillator performance are quantum efficiency and speed of each of the three stages of conversion, transport, and luminescence. Quantum efficiency is described by the simple multiplication of the singular efficiencies (all values between 0 and 1):

$$\eta = \beta S Q \quad (4)$$

where β , S and Q are the efficiencies of conversion, transport and luminescence, respectively.

Conversion efficiency, β , is a function of the energy required to produce an electron-hole pair. This in turn is a function of ionizing energy, and certain loss coefficients [31].

Ultimately, one can calculate the number of photons generated by a γ particle per MeV.

$$L = \frac{10^6}{2.3E_g} \beta S Q \quad (5)$$

A scintillator's speed is based on the rates of speed of the transfer and emission (or radiative) portion of overall scintillation, both with different speeds. The inverse of the slower rate is referred to as the decay time. A fundamental limit exists on the rate of emission. If one considers the dipole emission nature of radiation, then the radiative decay time in ns is [31]:

$$\tau_r = 1.5 * 10^{-5} \frac{\lambda^2}{f^{\frac{1}{9}}(n^2 - 2)^2 n} \quad (6)$$

2.4. Radiometry

Per Palmer, radiometry is "the measurement of optical radiant energy" [32]. One can track the radiant energy from one source or scene to another via the fundamental radiometric equation:

$$d^2\Phi = \frac{L dA_0 \cos \theta_0 dA_1 \cos \theta_1}{R^2} \quad (7)$$

The equation describes the radiant flux of one source onto a target as a function of a source radiance, projected area of both source and target divided by the square of the distance between them.

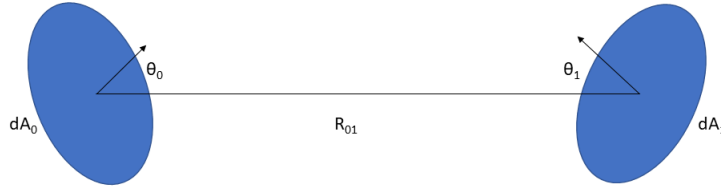


Figure 2-4 Radiometric Transfer adapted from [33]

The radiometric transfer equation can simplify to:

$$\Phi = LA\Omega \quad (8)$$

Recall both A and Ω are unprojected quantities and require the cosine projection factor should there be a viewing angle between source and target.

2.4.1. *Overview of Radiometric Nomenclature*

Several terms need to be understood in the process of understanding radiometry.

- **Radiant Energy**
Radiant energy is the fundamental quantity of energy from an electromagnetic wave. It has the unit of Joule.
- **Radiant Flux or Power**
Radiant flux is the fundamental energy quantity per unit time
- **Radiant Exitance**
Exitance is the radiant flux (power) emanating from a source. It is power per unit source area as radiating into a hemisphere.
- **Irradiance**
Irradiance is the power incident on a target. It is the radiant flux per unit target area.
- **Radiant Intensity**
Radiant intensity is the radiant flux (power) per unit solid angle.

- **Radiance**

Radiance is defined as the radiant flux (power) per unit projected area, per unit solid angle.

- **Throughput**

Throughput, or the $A\Omega$ product is the “geometric” reach of an optical system. It describes, in purely geometric terms, the amount of light (flux) that can travel through an optical system [33].

Term	Symbol	Units
Radiant Energy	Q	J
Radiant Flux or Power	Φ	J/s or W
Radiant Exitance	M	W/m^2
Irradiance	E	W/m^2
Radiant Intensity	I	W/sr
Radiance	L	$W/m^2/sr$

Table 2-1 Radiometric Nomenclature

2.4.2. *Lambertian Radiators*

Certain scintillators, like columnar scintillators in the presence of gamma rays are Lambertian in their radiance [34]. A Lambertian radiator is one whose radiance is not a function of angular position. Rather, the irradiance on a detector a distance R away would follow the cosine to the fourth law. Graphically, a Lambertian radiator’s emission is shown in Figure 2-5.

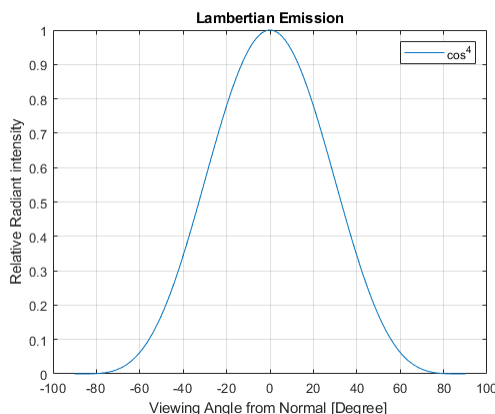


Figure 2-5 Lambertian Cosine Law

Specifically, the cosine law for Lambertian radiators is:

$$E = \frac{L_s A_s \cos^4 \theta}{z^2} \quad (9)$$

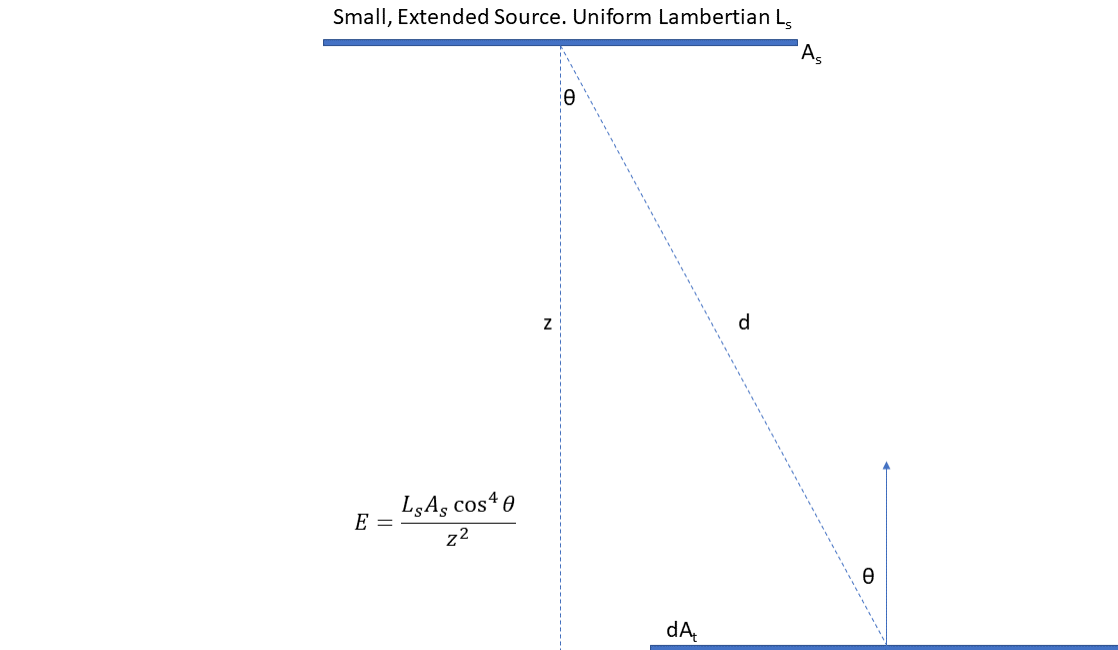


Figure 2-6 Lambertian Cosine Law

2.4.3. Radiometry of optical lens systems

One can estimate the throughput of an optical system using radiometric principles. Namely, the conservation of radiance states that the radiance of an optical system is the same anywhere along the optical track only if there are no losses present in the system. One can utilize the conservation of radiance when tracking the throughput in an optical system.

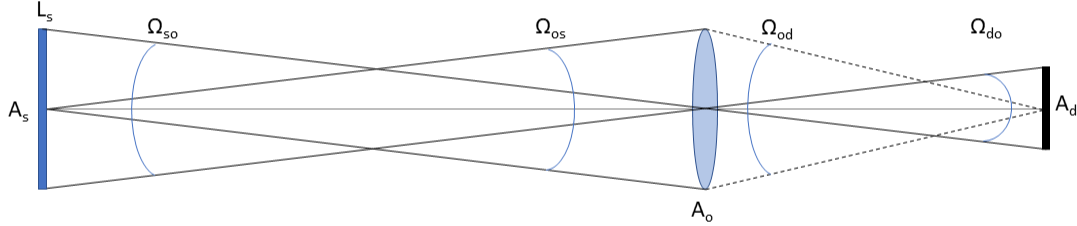


Figure 2-7 Radiometric Throughput adapted from Grant[35]

$$A_s \Omega_{os} = A_o \Omega_{so} = A_o \Omega_{do} = A_d \Omega_{od} \quad (10)$$

Consider a simple thin lens imaging a Lambertian surface onto a detector as in Figure 2-7. The throughput is conserved in an ideal, losses system and is constant. Throughput is defined for imaging systems as [33]:

$$T = n^2 A \Omega = n^2 \left(\frac{\pi f^2}{4F_\#^2} \right) \left(\frac{ab}{f^2} \right) = \frac{n^2 \pi ab}{4F_\#^2} \quad (11)$$

The radiometric throughput can also be expanded when ‘stitching’ together optical systems, as is the case in this thesis. The power incident on the detector can be the product of Equation 8 for each of the subsystems: front-end and back-end. When calculating the radiant flux (power) through one optical system into the next, the intermediate image plane will be used as the area of the detector (A_d in Figure 2-7) and A_o will be the area of the entrance pupil.

2.4.4. Radiometers

Radiometers are systems that measure light quantity emanating from a source or a scene. Ideally, a radiometer would be accurate and repeatedly measure the same quantity. Furthermore, the ideal

radiometer would have unity response over the wavelength(s) of interest. Several types of radiometers are realistic in practice. For example, the classic basic radiometer (Figure 2-8) is one that includes a single lens and a detector with the lens acting as the aperture of the system. Adding an aperture stop a focal length away from the lens allows the user to limit the field of view by limiting the ray bundle entering the system while also making the system telecentric, as is the case in Baudet [34].

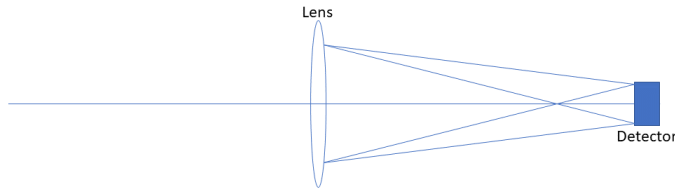


Figure 2-8 Basic Radiometer adapted from Palmer[32]

The irradiance on a detector from an isotropic source is defined as:

$$E_o = \frac{I_s \tau_{atmosphere}}{d^2} \quad (12)$$

Remembering that Irradiance (E) has the units of W/m^2 , one simply has to multiply by the lens area to obtain power on the detector considering transmission of the atmosphere and the lens itself.

$$\Phi = \frac{I_s \tau_{atm} \tau_{lens} A_{lens}}{d^2} \quad (13)$$

For an extended (Lambertian) source, I_s is defined to be:

$$I_s = L_s A_d \quad (14)$$

So the final power incident on the detector is just:

$$\Phi_d = \frac{L_s \tau_{atm} \tau_{lens} A_{lens} A_{det}}{f^2} \quad (15)$$

3. METHODOLOGY

3.1. Optical System with Fiber Relay

The new DYnamic SCintillator Optic (DYSCO) diagnostic must capture, by way of a scintillator, spatially resolved x-ray emission from an arbitrary source. The system must contain three distinct sub-systems: front-end, imaging fiber-cable relay, and back-end. The imaging fiber-cable relay will first be treated as a monolithic fiber of arbitrary length. The front-end will contain the scintillator. The back-end will include the camera sensor.

3.1.1. *Updated Radiometry Requirements*

1. Fiber Choice

Our fiber is Asahi Kasei's MBL-2000 plastic optical fiber (POF). The numerical aperture of the fiber is 0.5. Thus, a correctly coupled optical system matches the numerical aperture and so a system with a F-number of F/1, or an NA = 0.5 must be used. The fiber has 13,000 cores inside a 2 mm fiber bundle clear aperture. The core diameter is 15 microns. Including cladding, the fiber diameter is calculated to be 17.5 microns.

2. System Throughput Requirement

The throughput of an optical system is dependent on the magnification of the system.

$$T = \pi S N A^2 \quad (16)$$

The incident and outgoing NAs are also related via the magnification, M

$$N A_i = N A_o \sqrt{M} \quad (17)$$

The maximum incident NA of the front-end- that is, the maximum NA of the system facing the scintillator, is then:

$$N A_{fiber} \sqrt{M} = 0.5 \sqrt{0.2608} = 0.255 \quad (18)$$

$$F/\# = 1.96 \quad (19)$$

The maximum incident Numerical Aperture of the back-end - that is, the maximum NA of the system facing the sensor- is then

$$N A_{fiber} \sqrt{M} = 1 \sqrt{2.183} = 1.477 \quad (20)$$

$$F/\# = 0.34 \quad (21)$$

Thus it does not make sense- to have a system faster than F/1.

3.1.2. Updated Optical Requirements

The derivation of requirements is as follows.

1. Wavelength

P43 and P47 phosphors are the scintillator options for use in this diagnostic. P47 emits at 400 nm with a decay time of 70 ns. P43 emits at 550 nm with a decay time of around 1 ms. The primary wavelength will be 400 nm and the system will be designed monochromatically.

2. Resolution

The derivation of requirements will begin with the sensor. The system will be imaged by a Princeton Instruments' PI-MAX4 1024i Intensified CCD Camera. This sensor has 1024x1024 pixel array which contains 12.8 micron-sized pixels to complete a 13.1 mm rectangular image plane, or 18.5 mm diagonal chip. The cutoff frequency associated with this pitch is:

$$f_c = \frac{1}{d} = \frac{1}{12.8\mu m} = 78mm^{-1} \quad (22)$$

Note that the resolution of the system is also affected by the resolution of the fiber. The fiber in use is from Asahi Kasei P/N: MBL-2000 and is a multicore plastic optical fiber with 13000 cores comprising a 2mm diameter fiber bundle. Those 2mm fiber bundles are then formed into a ‘super-bundle’ formed of 7 fiber bundles, called a ‘rosette’.

3. Numerical Aperture and F/#

The numerical aperture is defined by real rays, and thus, is an appropriate variable to specify. Note that the optical fiber has an NA of 0.5. Radiometry constrains the NA of the front- and back-ends to match the fiber.

The F/# is given by the first-order relationship:

$$F/\# = \frac{1}{2 * NA} = \frac{1}{2 * 0.5} = 1 \quad (23)$$

$$F/\# = \frac{f}{D_{EntrancePupil}} \quad (24)$$

4. Entrance Pupil Diameter

With the NA of the back-end system driven to be 0.5, this fast speed can only be accomplished if broader lens diameters are used. A reasonably achievable diameter is 2 inches:

$$EPD = 50.8mm \quad (25)$$

5. Focal Length

The focal length is then driven to be the same dimension to satisfy equation (24):

$$f = 50\text{mm} \quad (26)$$

6. Field of View

The back-end images a 6 mm diameter fiber face onto an 18.5 mm diagonal chip.

7. Magnification

The Back End shall image the fiber onto the 18.5 mm diagonal (13.1 mm side length) chip.

$$m_{BE} = \frac{h'}{h} = \frac{13.1\text{mm}}{6\text{mm}} = 2.183 \quad (27)$$

8. Telecentricity

According to Fan et. al.[36], both front- and back-end systems should be telecentric in the space facing the optical fiber. Namely, the front-end to be telecentric in image space and the back-end to be telecentric in object space.

3.1.3. *Updated Opto-Mechanical Constraints*

In order to fit within the Z-Containment vessels the front-end must be made smaller than the existing DISCO front-end and have a right-angled bend. Thus, the DYSCO front-end will have (1) a fiber-taper to collect and reduce the optical image from the scintillator, (2) a 90° fold mirror to redirect the image vertically, and (3) a new set of smaller lenses to couple the image to the imaging-fiber-cable. The DYSCO back-end must fit within the clear aperture of the PIMAX 1024i camera and utilize the F-mount adapter.

3.2. *Front-End Optical Design*

The front-end lens design for the DYSCO diagnostic system is presented here. It consists of three parts: a collection of lenses, a fold mirror, and a commercially available fiber taper (Edmund Optics). The collection of lenses couples the 8 mm fiber taper exit face to 6 mm fiber bundle entrance face. Because of the L-bend due to the fold mirror, this front-end version is referred to as DYSCO-L.

3.2.1. *Lens Design*

Lens design for the purpose of imaging objects or scenes is both an art and a science. It requires knowledge of fundamental design forms that are then iterated upon to form unique solutions given several design criteria. Historically, imaging applications were to assist in painting art as in the case of Johannes Vermeer. The ray-based understanding of imaging would translate to a point source being imaged to a point. Furthermore, if an object were to have a planar extent, the image

would also reside in a perfect plane. Finally, the magnification, which is defined to be the ratio of the image height and the object height, would be conserved over the entire image plane. That is, the magnification would be the same for every pair of points on the image and object plane [37]. Aberration theory and the wave nature of light declares that every one of these idealizations is untrue. For example, an electromagnetic wave originating from a point source and traveling through a finite aperture (say a lens diameter) will diffract into a small disk on the image plane, called the Airy disk. Secondly, an object with a discrete height inside the object plane has a longer distance to the lens than the on-axis case. Gaussian imaging dictates the image distance would be slightly outside of the on-axis image plane. An object plane of discrete height images onto a curved image surface. Finally, magnification can grow linearly with the object height. That is, the magnification of one object height is different than another object. This describes distortion aberration.

Several other imaging aberrations exist including defocus, spherical, coma, astigmatism, Petzval field curvature, aforementioned distortion, and the chromatic aberrations of chromatic change of focus and chromatic change of magnification, not to mention the higher order aberrations that are intrinsic to the fact that an object has a height or that a pupil has some discrete size. Thus the optical lens designer must deploy aberration mitigation techniques in order to form an image that exceeds some specification. Some design forms are best suited to an application, depending on field of view and numerical aperture criteria. For example, the design form used in this thesis centers on a Petzval portrait lens as the number of surfaces allow for correction of spherical, coma, and astigmatism. A field flattener lens may be added to correct for Petzval field curvature.

3.2.2. *Optical Parameters*

The design goals for the DYSCO-L front-end lens collection system are described in Table 3-1.

Parameters	Values	Units	Comments
'Pixel' Size	15	μm	fiber core diameters
Numerical Aperture	0.5		in Image Space
Total Track Length		mm	System must have a right-angle L bend to fit inside Containment
FOV	± 12.5	mm	In Object Space
Magnification	-0.75		Lens system magnification not including the fiber taper
Wavelength	405	nm	
Distortion	< 5	%	
Telecentricity			Telecentric in Image Space

Table 3-1 Compliance Matrix of the DYSCO Front End

3.2.3. *Design Overview*

The design process was to use the ‘building block’ approach to lens design. That is, to independently design an ‘objective’ and an ‘eyepiece’ suitable for the application and ‘stitch’ the resultant portions together. Additionally, a fiber taper would be used to image a 25 mm object to an 8 mm image. Thus, the DYSCO-L overall magnification is 0.25 (25 mm object to 6 mm image) but the lens system itself only requires a magnification of 0.75 (8 mm object to 6 mm image).

Ideally, a 25:6 mm fiber taper would be used instead of a 25:8 fiber taper. Unfortunately, only the 25:8 fiber taper is commercially available by SCHOTT via Edmund Optics. Custom 25:6 fiber tapers have been requested, but will not be available for the completion of this thesis

3.2.4. *Objective*

The objective was chosen to be the portion with the L bend. A perusal of the Zemax OpticStudio design templates was performed with the criterion that an objective has at least one long inter-lens distance so as to place a fold mirror. One such design was a small format objective based on USP 3961844 as shown in Figure 3-1.

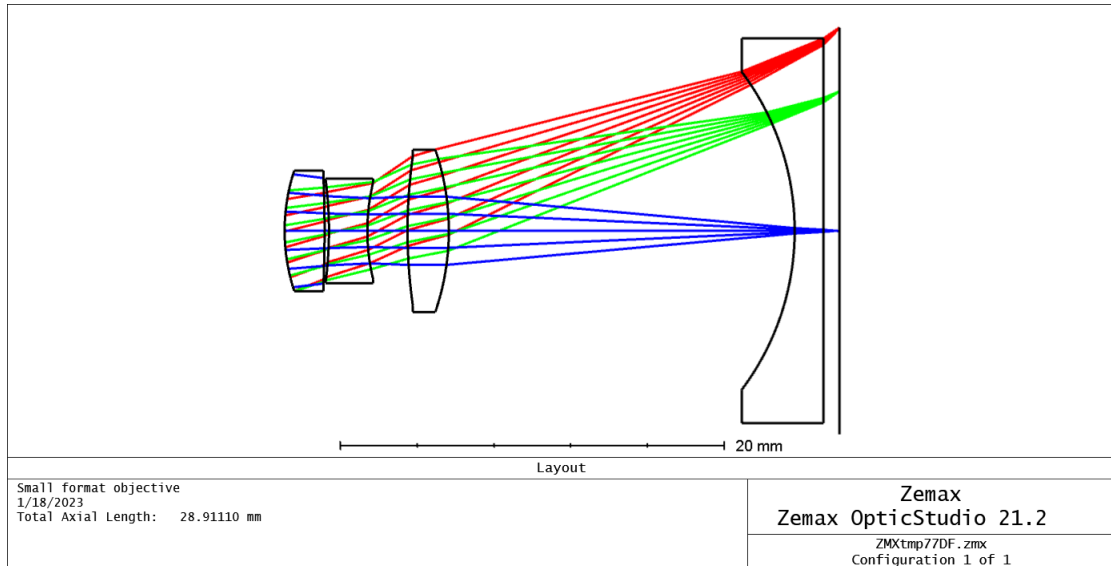


Figure 3-1 DYSCO-L Front End Starting Point Layout from USP 3,961,844

This Cooke Triplet and field flattener combination demonstrated the inter-lens distance required to insert a fold mirror. The image plane of this portion would couple to the fiber taper's 8 mm face. Note the external stop.

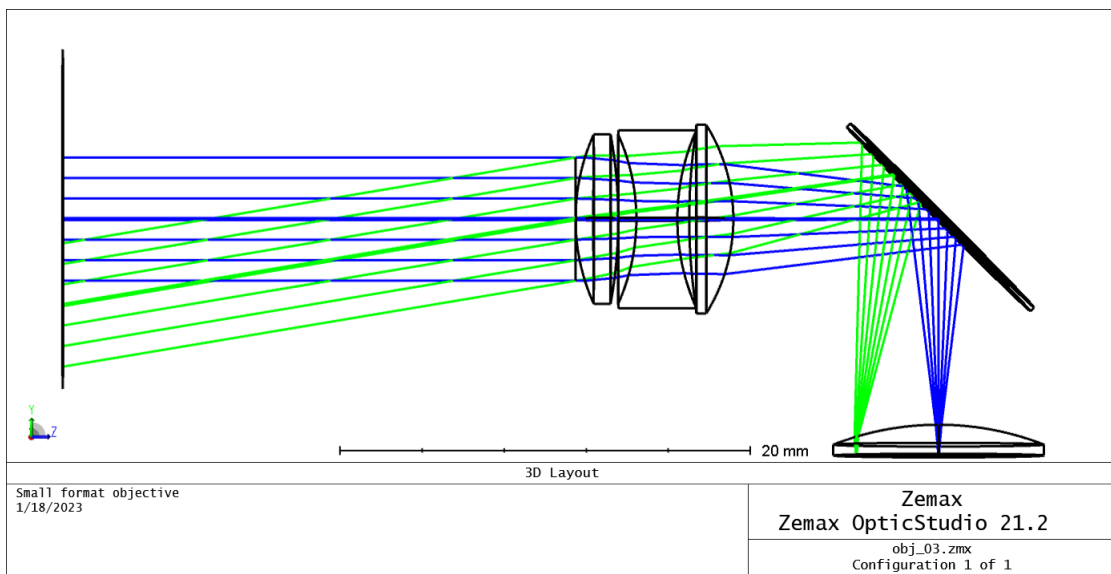


Figure 3-2 DYSCO-L Front End with fold mirror inserted

Figure 3-2 shows the folded objective portion with a 4 mm real image height field definition (recall image height in raytracing software is the radial height). This objective portion was then coupled with the eyepiece.

3.2.5. Eyepiece

The ‘eyepiece’ was the portion that faced the 6mm diameter (3mm radial) fiber bundle clear aperture. A search through the Design Template Library yielded the following system from Laikin (Laikin, Figure 10-3 [38]). It is common practice to design lenses ‘backwards’ for simplicity. It was reversed in the next stage of the design.

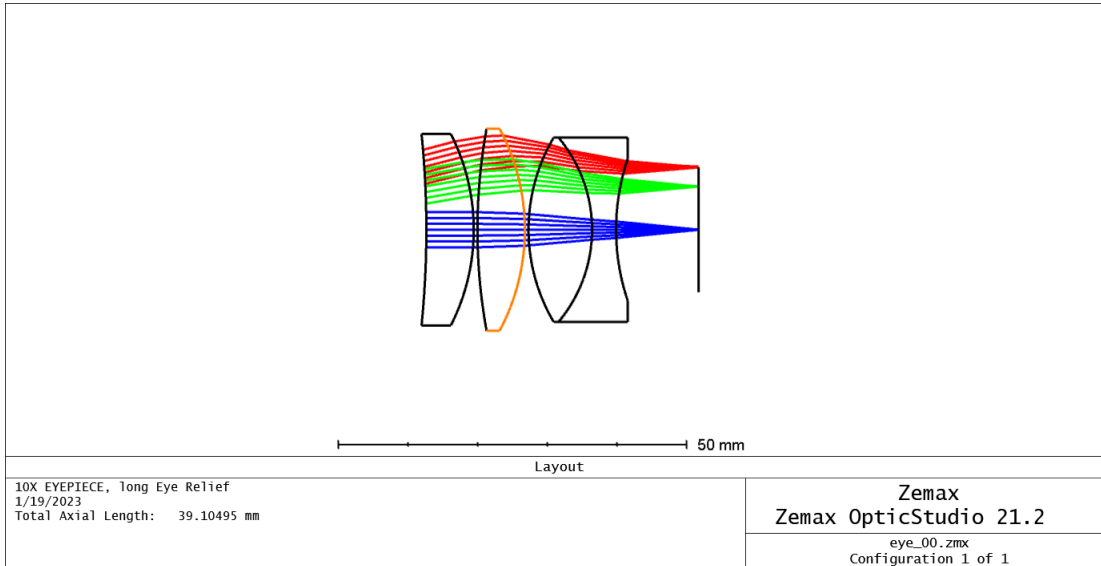


Figure 3-3 DYSCO-L Front End Eyepiece starting point from Laikin [38]

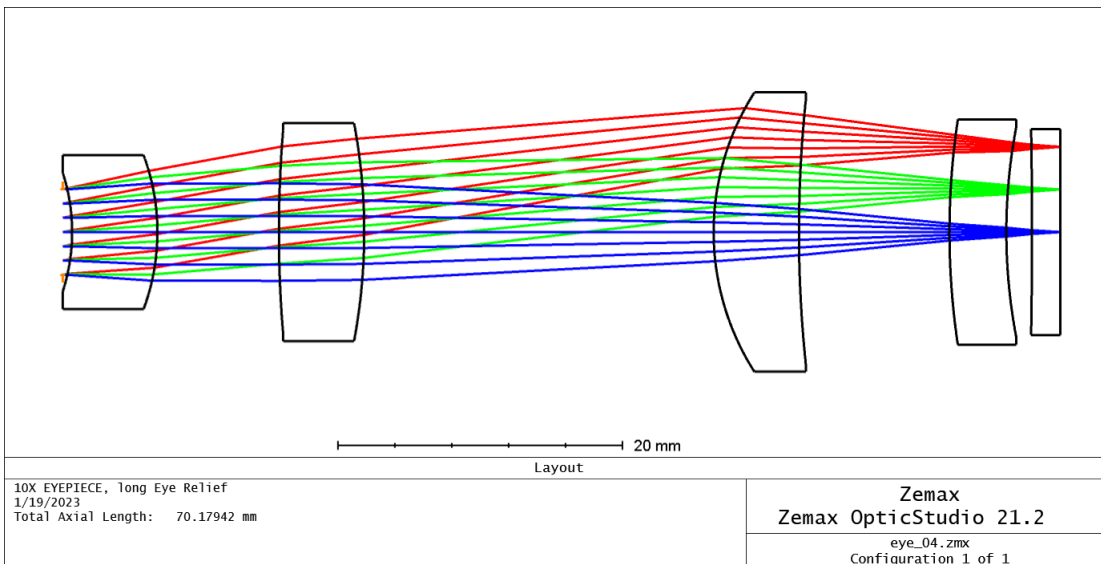


Figure 3-4 DYSCO-L Front End Eyepiece.

A field flattener was introduced, and the doublet split to address field curvature and spherical aberration, respectively. Note the external stop.

3.2.6. Combination

Before stitching together the ‘eyepiece’ with the ‘objective’, the individual portions must have external stops of the same size. Both systems have an aperture of 6 mm.

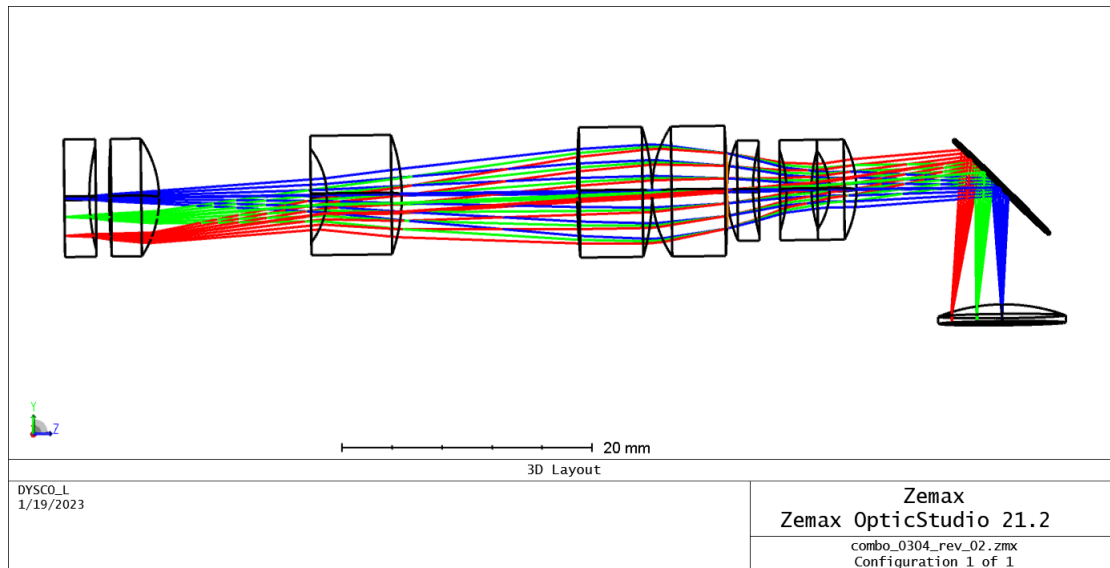


Figure 3-5 DYSKO-L Final combination. Here light travels from bottom right to left.

3.3. Back-End Optical Design

The DYSKO back-end is the fiber-to-camera lens coupling system portion of the DYSKO diagnostic.

3.3.1. Optical Parameters

The design goals for the Back End system are described in Table 3-2 :

Parameters	Values	Units	Comments
Pixel Size	12.8	μm	
Numerical Aperture	0.5		in Object Space
Total Track Length		mm	
FOV	± 3	mm	In Object Space
Magnification	-2.183		
Wavelength	405	nm	
Distortion	< 5	%	
Telecentricity			Telecentric in Object Space

Table 3-2 Compliance Matrix of the DYSCO Back End

3.3.2. *Design Overview*

The design process was to use objectives and common design forms as building blocks that could be combined to provide a workable solution for our application. As mentioned in Section 3.1.2, the system had to meet several requirements. A compliance matrix is shown in Table 3-2.

The back-end optical design strategy followed the modular approach of optical design. Namely, objectives and eyepieces would be designed separately, and later combined to form the final system. Three candidate designs were found and evaluated all with the same objective but with different eyepieces.

3.3.3. *Objective*

The Numerical Aperture of the objective needed to be relatively high at 0.5 to match the NA of the fiber. In addition, the design needed to be telecentric in the space facing the fiber (for the back-end, in object space). Several design forms can achieve high performance at such a high optical speed albeit with a low field of view. The Petzval Lens is one such design form. The starting point design was William Schade's Petzval Lens (US Patent 2,158,202). The fast speed was achieved through several design iterations of shortening the focal length and broadening the entrance pupil. Next the lens was made to be telecentric in object space. Finally, the lens was scaled to produce the desired field of view. Since the objective will face the fiber, a ± 3 mm field of view was specified and re-optimized. All the lenses were designed to be <50 mm in diameter.

3.3.4. *Eyepiece*

Several eyepiece options were considered, discussed below.

1. Petzval Lens

One option was the Petzval lens similar to the objective. Usually comprised of two achromatic doublets (split or cemented) and a field flattener, the Petzval lens can be fully corrected for all primary aberrations including field curvature and distortion [39].

2. Double Gauss

The second starting point was the Double Gauss lens. Double Gauss lens forms are favorable because of their intrinsic symmetry (hence low distortion) and because they're a relaxed lens and the tolerances can be loose. When making a Double Gauss telecentric, the field of view must decrease.

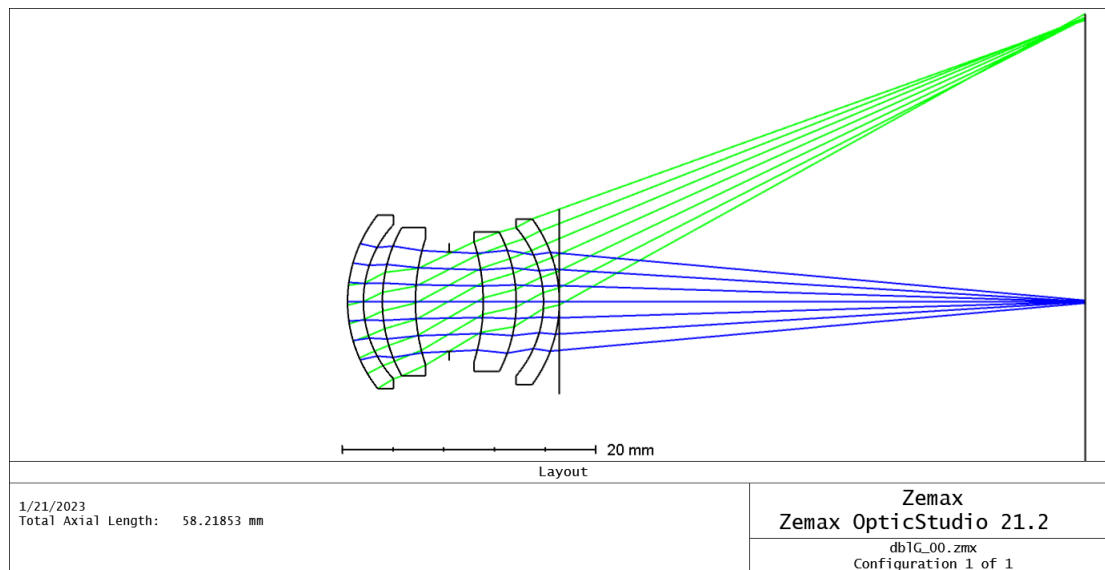


Figure 3-6 DYSKO Back End Starting point: Classic Double Gauss

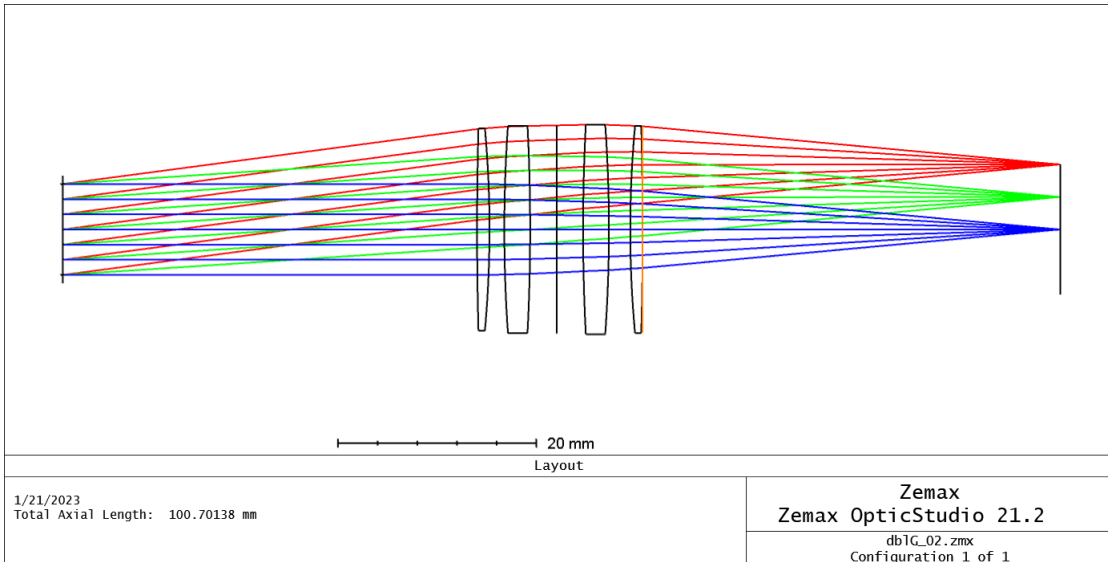


Figure 3-7 DYSCO Back End Eyepiece candidate: telecentric Double Gauss

3. Cooke Triplet

The final option considered was a Cooke Triplet. While it may also have symmetric qualities, the fewer number of surfaces means the Cooke Triplet design form has tighter tolerances. Again, telecentricity forces a compromise with field of view.

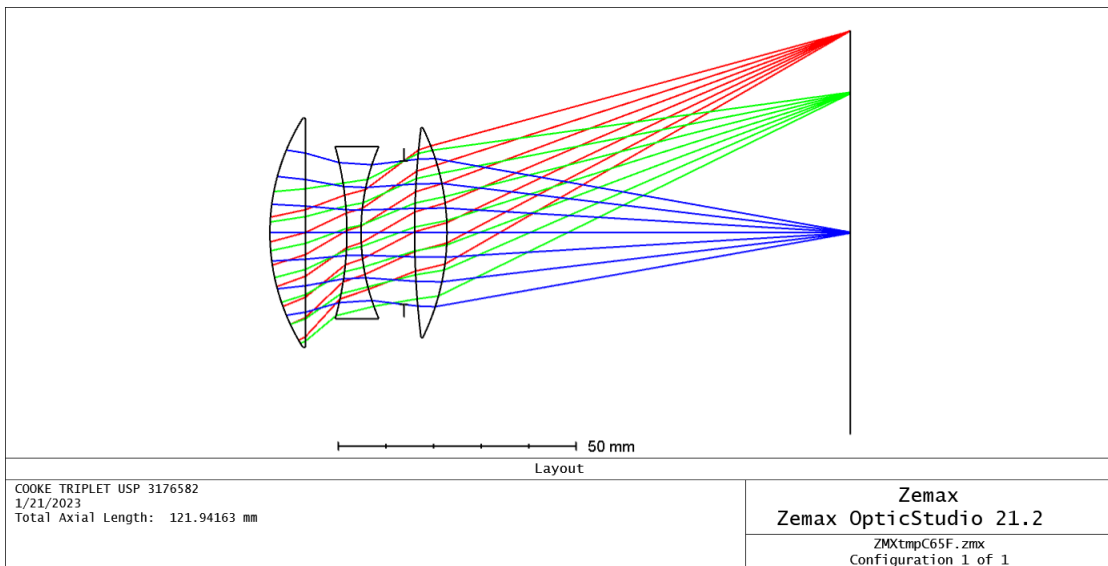


Figure 3-8 DYSCO Back End Starting point: Classic Cooke Triplet USP 3176582

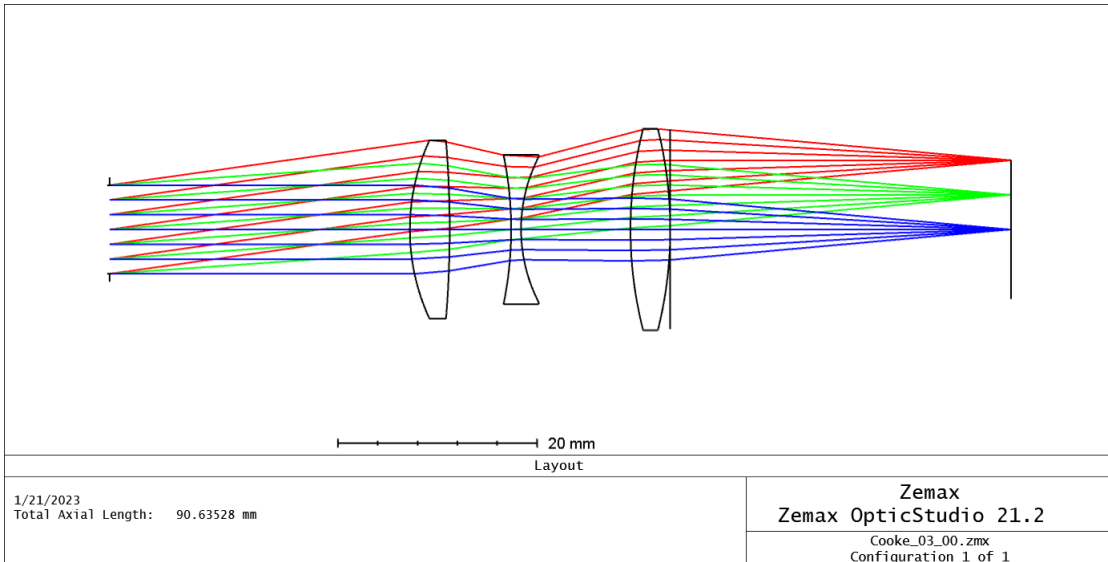


Figure 3-9 DYSCO Back End Eyepiece candidate: telecentric Cooke Triplet

3.3.5. Combination

The winning design was the Double Gauss derivative as this design was most insensitive to tolerances from the three eyepiece candidates. Results of the solution are found in the Results section.

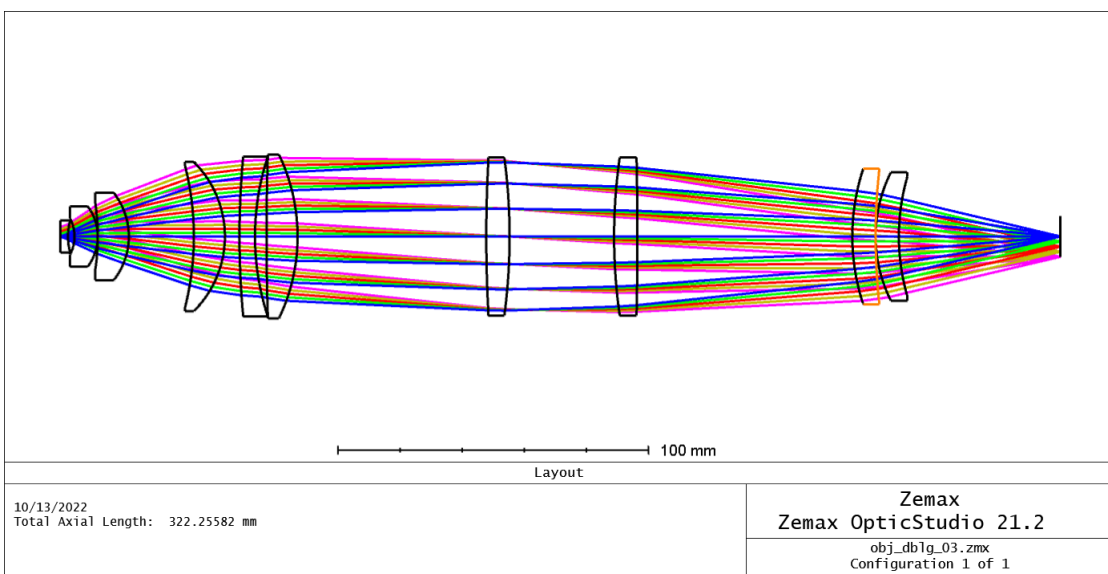


Figure 3-10 Winning DYSCO Back End Layout

3.4. Radiometry

The radiometry of the system will be treated as we try to ascertain the throughput of the entire system. Ultimately, we will estimate how much signal exists per keV of X-ray input energy. This must begin with the conversion efficiency of the scintillating phosphor.

3.4.1. Radiometry of Coupled Optical Relay Systems

- **First Order Calculation**

One can estimate the throughput of the front-end by treating the front-end system as a simple thin lens model. (See Equation 6.33 from Willers [33]).

$$T = n^2 A_{optics} \Omega_{fov} = n^2 \left(\frac{\pi f^2}{4F_\#^2} \right) \left(\frac{ab}{f^2} \right) = \frac{n^2 \pi ab}{4F_\#^2} \quad (28)$$

3.4.2. Front-End Radiometry

- **Hand Calculation**

For the front-end system noting the ‘image detector plane’ is circular and using the ‘image’ side F-number,

$$T = \frac{n^2 \pi ab}{4F_\#^2} = \frac{(1)^2 \pi^2 (6mm)^2}{(4)(1)^2} \quad (29)$$

$$= 9\pi^2 * 10^{-6} m^2 sr \quad (30)$$

- **Zemax OpticStudio Simulation**

An estimate of system light transmission is available as an OpticStudio calculation by going to the Analyze tab > Polarization > Transmission.

For unpolarized input light, the transmission of the DYSCO-L front-end subsystem is 80%. Note that all the surfaces have appropriate coatings for the wavelength of interest.

3.4.3. Fiber Radiometry

Per the manufacturer, the POF has losses of 200 dB per km at 400 nm. At 10 meters of length, we can expect 2 dB of signal loss due to the fiber attenuation.

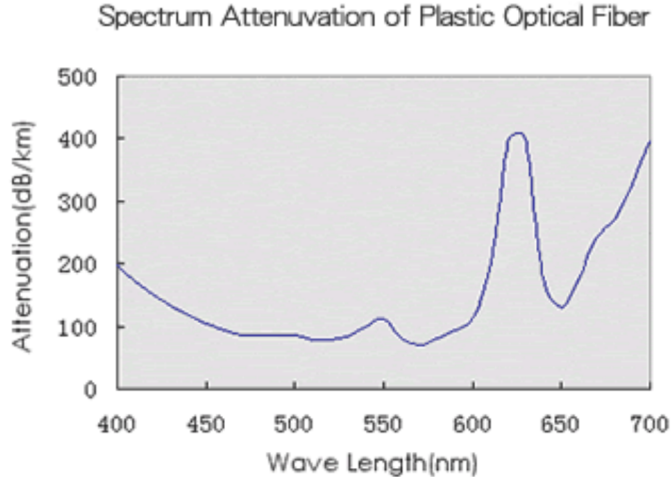


Figure 3-11 POF Fiber Attenuation curve per Asahi Kasei.[Link] [40]

3.4.4. Back-End Radiometry

- **Hand Calculation**

The throughput of the back-end, noting that the sensor plane is square and using the ‘image’ side F-number,

$$T = \frac{n^2 \pi ab}{4F_{\#}^2} = \frac{(1)^2 \pi (13.1\text{mm})^2}{(4)(2.2)^2} \quad (31)$$

$$= 8.86\pi * 10^{-6} \text{m}^2 \text{sr} \quad (32)$$

- **Zemax OpticStudio Simulation**

An estimate of system light transmission is available as an OpticStudio calculation by going to the Analyze tab > Polarization > Transmission. For unpolarized input light, the transmission of the Back End subsystem is 85%.

3.5. Radiance Characterization Experiments

The radiometer designed and used by Baudet [34] was rebuilt using new hardware to perform the scintillator radiance characterization experiments. The purpose of the experiments was to ascertain the radiance profile of the scintillator used in the DYSCO diagnostic system. The fundamental assumption was that the scintillator would have a Lambertian distribution, but needed to be verified via these experiments.

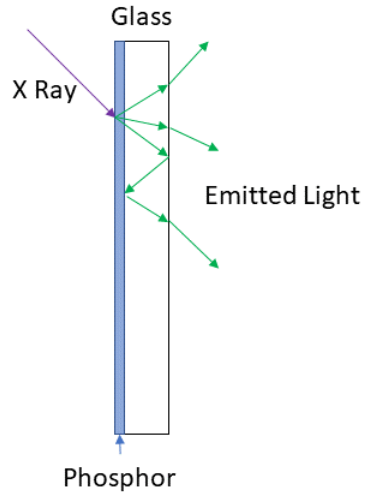


Figure 3-12 Scintillator operating at large angle of incidence may not be Lambertian.

Note the scintillator is a phosphor material coated on a glass substrate. The internal reflections of light inside the glass may cause the distribution of light to deviate from Lambertian.

The details of the radiance characterization setup are found in Ref. [34] but some details are elucidated here.

The radiometer is basically a one-lens radiometer with an aperture stop at the rear focal point of the lens. While also making the system telecentric, the stop position also limits the off-axis rays that can pass through the system and thus only a narrow cone of light is ‘considered’ when making a measurement at a particular angular position of the scintillator.

Note that the setup is to be telecentric in object space as the aperture stop is placed one focal length away from the lens. The setup must be telecentric so as to ensure “... the aperture of the system is constant across the detector area” [34].

The on-axis case is shown in Figure 3-13. The scintillator will be rotated about the field stop’s axis to ascertain the irradiance angular behavior. Once the irradiance behavior is known, the radiance characteristics can be calculated.

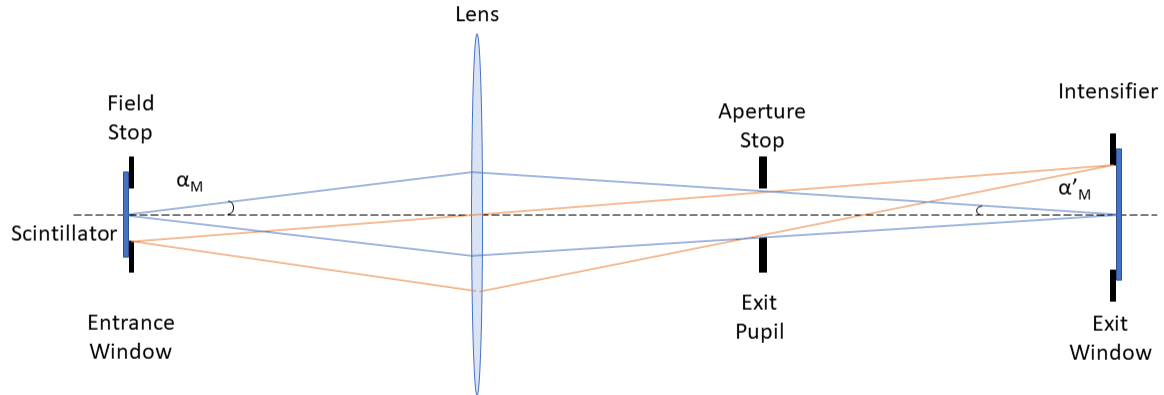


Figure 3-13 Geometry of radiometer per Baudet [34]

3.5.1. *Derivation of Gaussian Imaging Distances for The New Setup*

Recall that numerical aperture is defined as follows:

$$\text{NA}_{obj} = \sin \alpha_m \quad (33)$$

$$\text{NA}_{im} = \sin \alpha'_m \quad (34)$$

and F-number is defined as

$$F/\# = \frac{1}{2 \sin \alpha'_m} \quad (35)$$

From Figure 3-13, we calculate the diameter of the stop, assuming the lens limits the ray bundle through the radiometer.

$$\tan \alpha_m = \frac{D_{stop}}{2f'} \quad (36)$$

$$D_{stop} = D_{lens} \frac{m}{m-1} = (50.8 \text{ mm}) \frac{-2}{-2-1} = \mathbf{33.86 \text{ mm}} \quad (37)$$

The appropriate stop diameter to maintain imaging characteristics from Ref. [34] is given in Equation 37.

Recall the fundamental imaging equation:

$$\frac{1}{z'} = \frac{1}{f} + \frac{1}{z} \quad (38)$$

And recall the magnification relationship between object and imaged distances:

$$m = -\frac{z'}{z} \quad (39)$$

Combining equations 38 and 39 yields:

$$1 = \frac{z'}{f} + m \quad (40)$$

and solving for z' :

$$z' = f(1 - m) \quad (41)$$

For the recreated setup, the magnification will remain $m = 2$, and the focal length of the lens will be $f = 75 \text{ mm}$. Thus, based on equations 38 and 41, our object and image distances should be $z' = 225 \text{ mm}$ and $z = -112.5 \text{ mm}$.

3.5.2. **Setup**

All distances are relative to the scintillator plane. The scintillator was placed on a 3D-printed holder designed by Baudet for her experiments. The 3D-printed parts consist of a base plate, an aperture, and a triangular plate among others that held the rotating elements (See Figure III.3.3 from Ref. [34]).

The key deviations from Baudet include the choice in camera (a FLIR Grasshopper3 GS3-U351S5M) and the choice in intensifier (Proxitronic detector systems).



Figure 3-14 FLIR Camera Grasshopper 3 used in the experiment

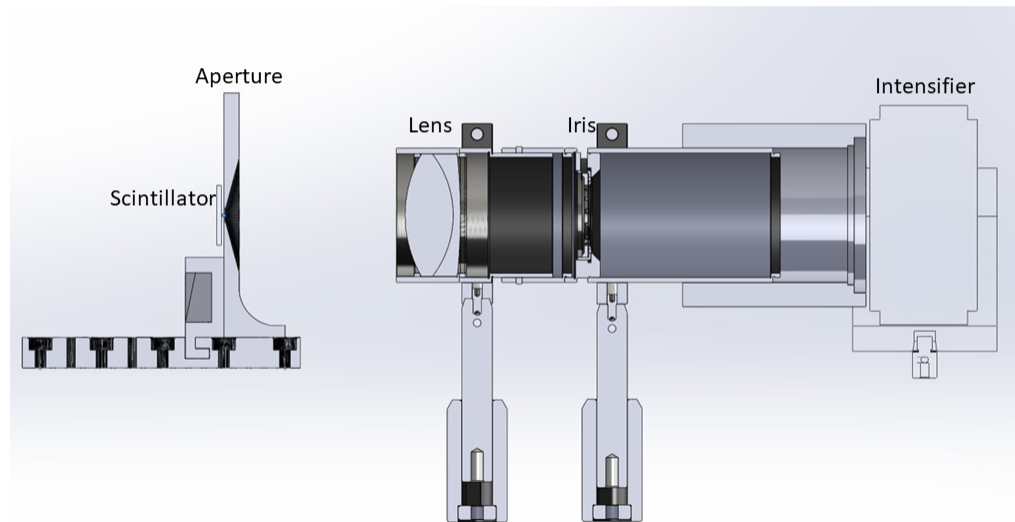


Figure 3-15 Radiance Characterization Setup. Not shown is the SolidWorks model of the camera and camera extension tubes used in capturing the final data.

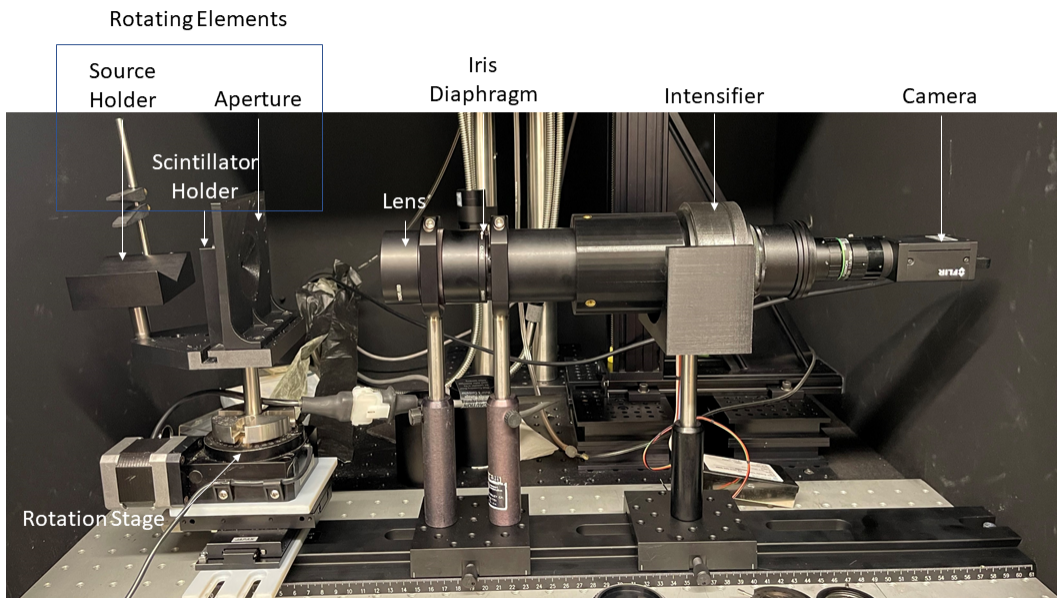


Figure 3-16 Radiance Characterization Setup.

4. RESULTS AND ANALYSIS

4.1. DYSCO Front-End Variants

The lens system for DYSCO-L (front-end) is Containment compatible. The extent of the first lens to the end of the mirror will fit radially inside the containment vessel (roughly 8 inches in diameter). Figure 4-1 shows the concept of DYSCO-L front-end in containment.

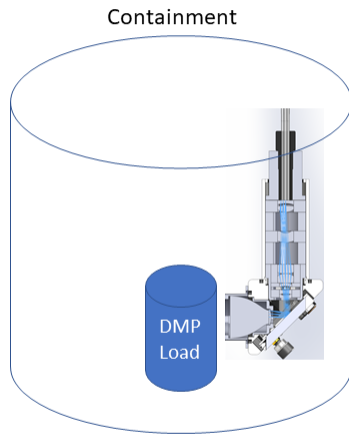


Figure 4-1 DYSCO-L shown inside the containment vessel (not to scale).

4.1.1. *Optical Performance Metrics*

1. Layout

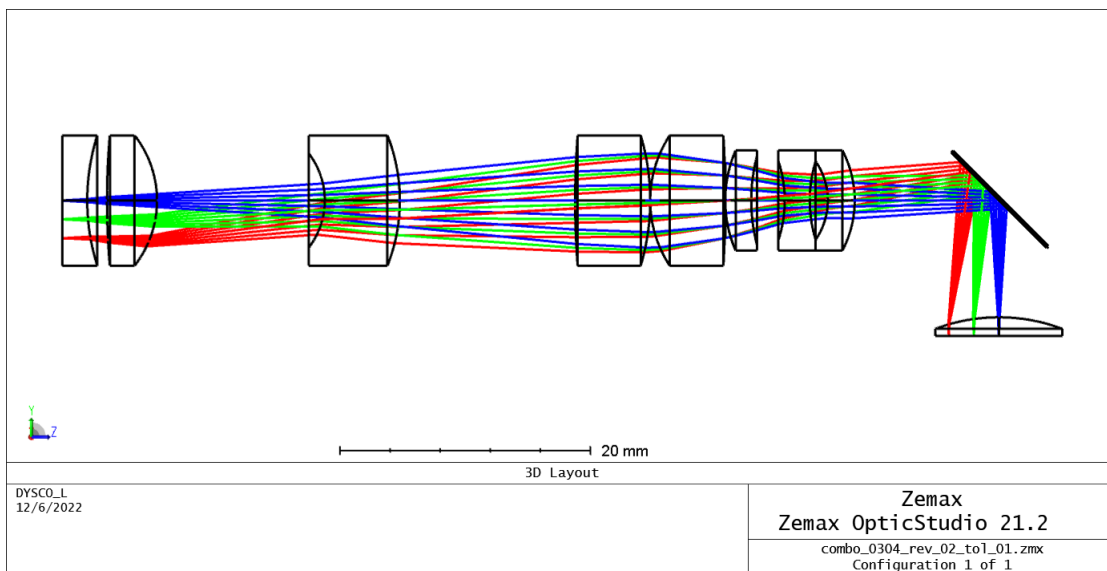


Figure 4-2 DYSCO Front-End Layout. Here light travels from right to left. The leftmost lens couples with the fiber and the lens facing up couples with the fiber taper.

Basic optical design theory states that a folded system can be unfolded with no loss in

optical image quality. The optical path taken in a ‘straight’ version matches the folded version. Figure 4-3 shows the variant called ‘DYSCO-Straight’.

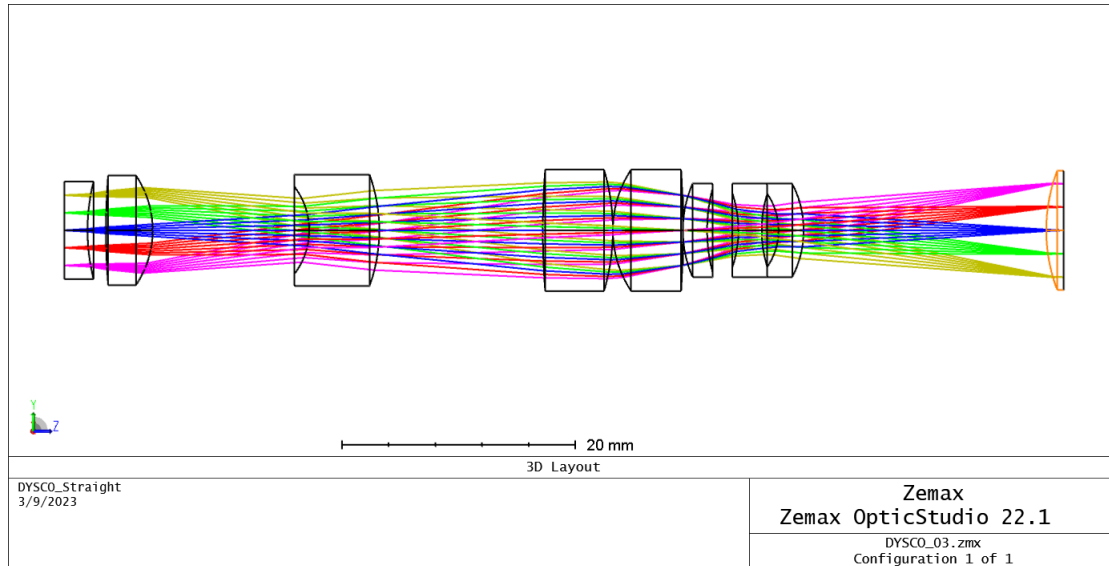


Figure 4-3 DYSCO Straight Front-End Layout. Here light travels from right to left. The leftmost lens couples with the fiber and the rightmost lens couples with the fiber taper.

While the optomechanical design does not fall under the purview of this thesis, a quick mockup of a potential DYSCO-L optomechanical design was performed.

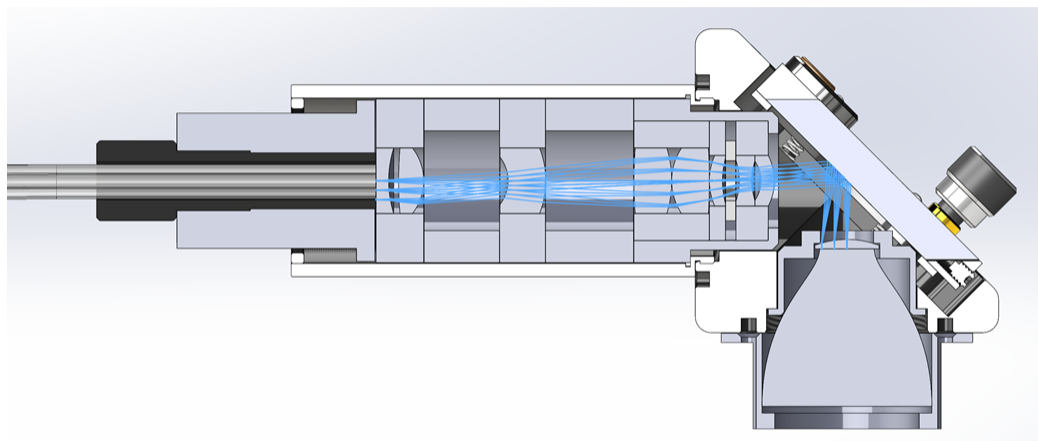


Figure 4-4 DYSCO-L Front-End Optomechanical Layout

A quick prototype lens assembly of the DYSCO Straight variant was built in the lab using 3D printed radial lens rings ('poker chips') and spacers.

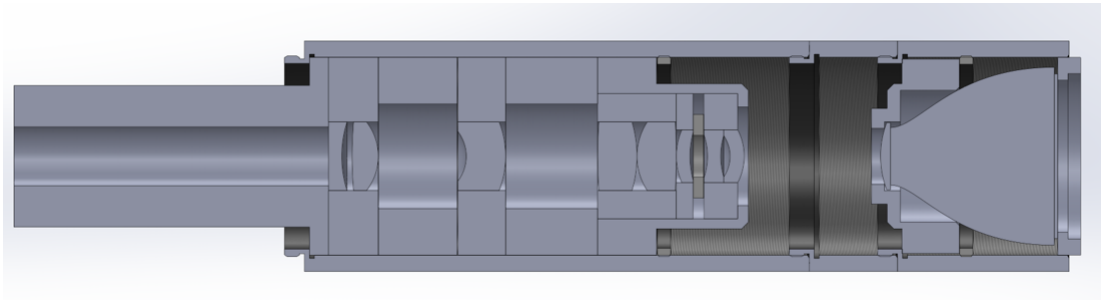


Figure 4-5 DYSCO-Straight Front-End Optomechanical Layout.

2. Spot Size

The spot size will fit within the 15-micron diameter core of the Plastic Optical Fiber.

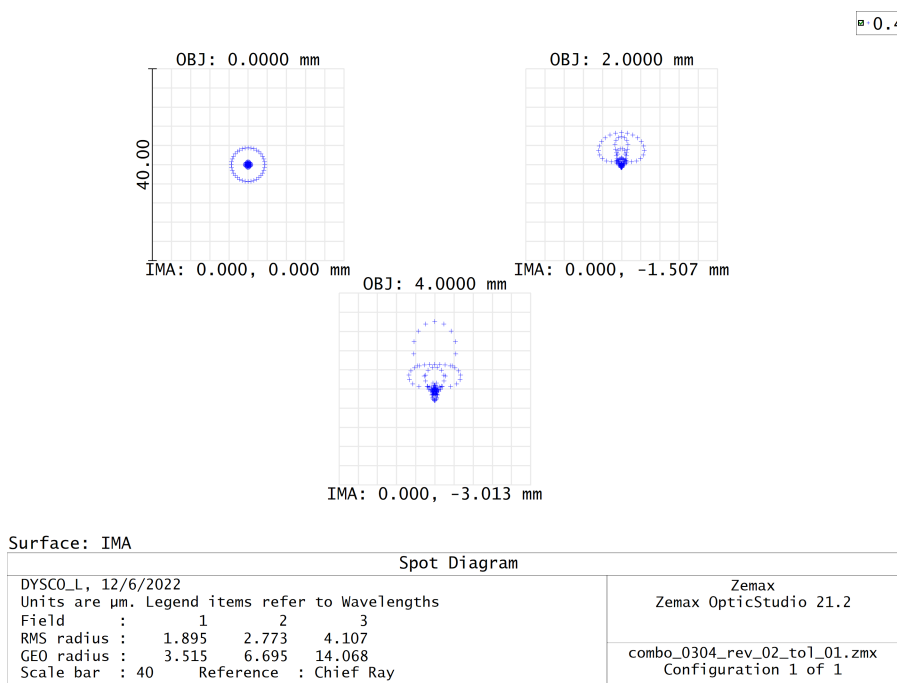


Figure 4-6 DYSCO-L Front-End Spot Diagram

3. Wavefront Error

The Optical Path Difference plots show residual aberration on the order of half a wave. At 400 nm, the largest wavefront error is less than 200 nm.

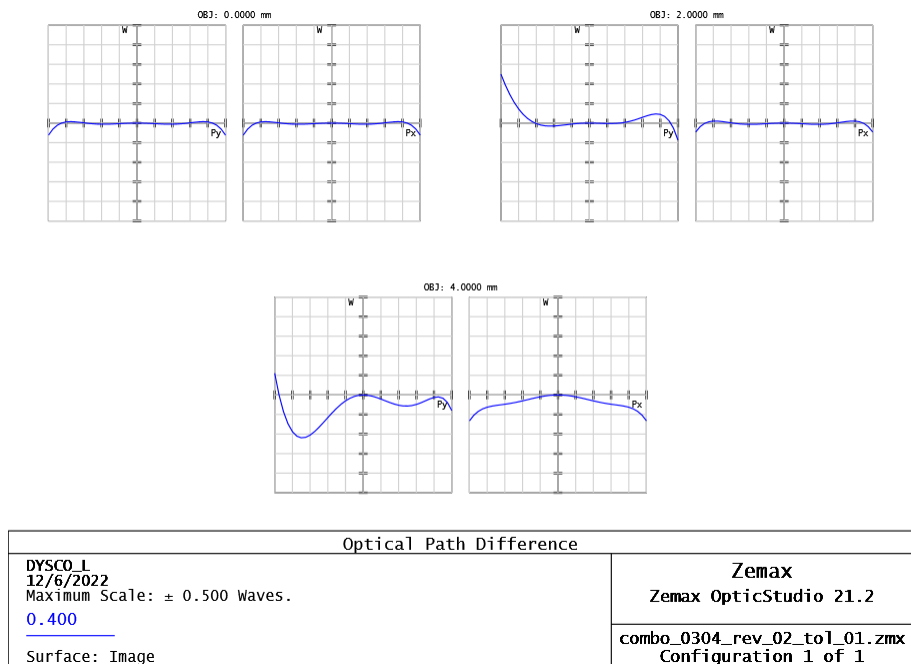


Figure 4-7 DYSCO-L Front-End Wavefront Error

4. Resolution

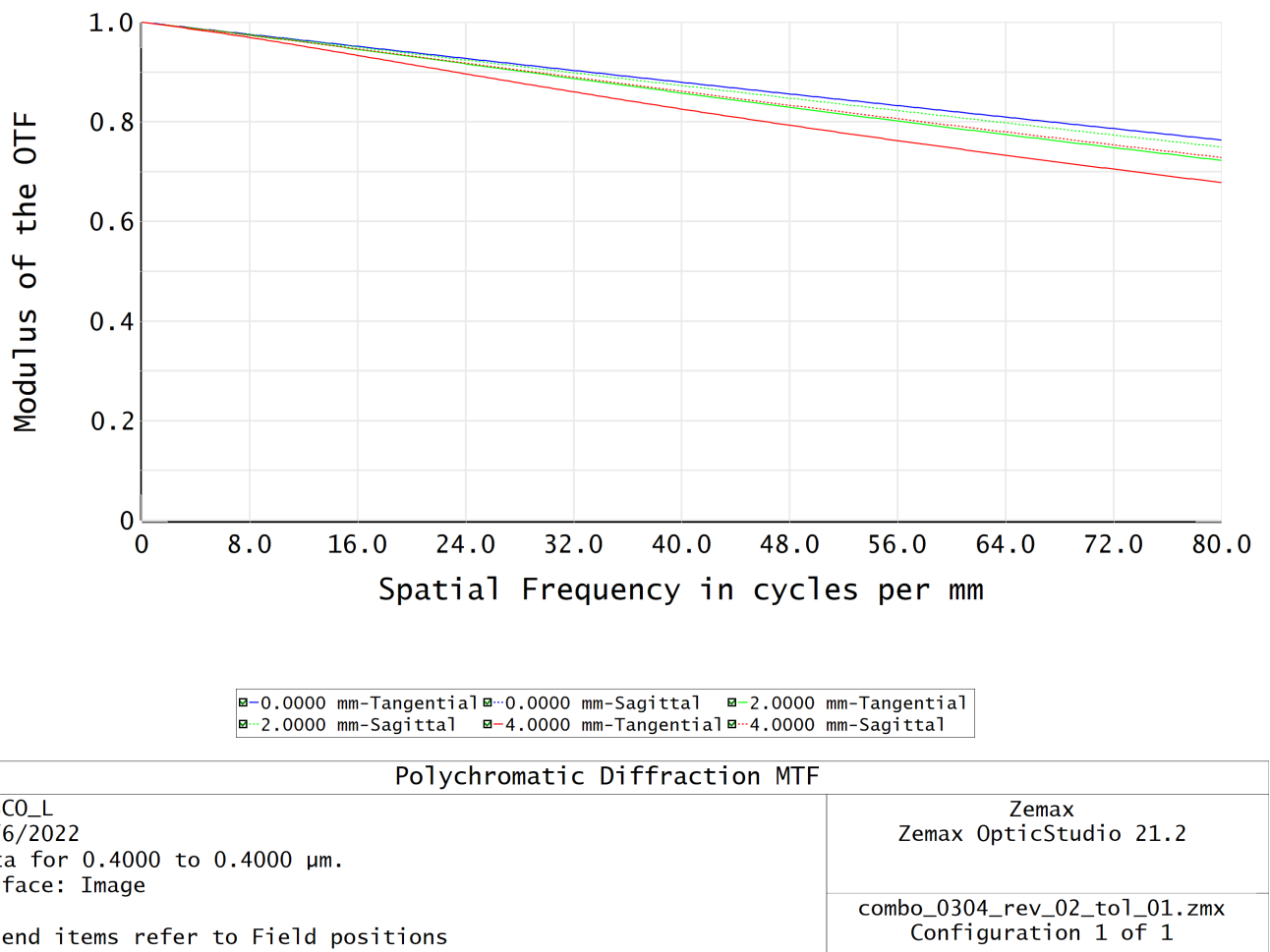


Figure 4-8 DYSCO-L Front-End MTF Resolution Chart

5. Image Simulation and Lab Capture



Image Simulation: Geometric Aberrations	
DYSCO_L 12/6/2022 Object height is 6.0000 Millimeters. Field position: 0.0000 mm Center: chief ray Image size is 4.5202 W x 4.5202 H (Millimeters)	Zemax Zemax OpticStudio 21.2
	combo_0304_rev_02_tol_01.zmx
	Configuration 1 of 1

Figure 4-9 DYSCO-L Front-End Image Simulation

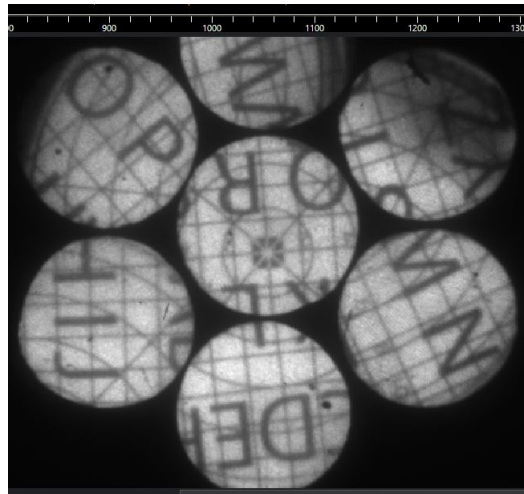


Figure 4-10 Raw DYSCO-Straight Front-End Image Lab Capture.

4.1.2. *Tolerancing Analysis*

Zemax OpticStudio allows several preset tolerance values for analysis. ‘Loose’ (commercial), ‘Standard’ (precision), and ‘Tight’ (high precision) tolerances can be selected based on manufacturer. The chosen tolerances were a combination of Edmund Optic’s Precision tolerances and custom element tilts and decenters. The complete tolerance list is displayed in Table 4-1.

Parameter	Values	Units	Comments
Radius	3	<i>fringes</i>	
Thickness	0.05	<i>mm</i>	
Surface Decenter X	0.2	<i>mm</i>	
Surface Decenter Y	0.2	<i>mm</i>	
Surface Tilt X	0.0333	<i>degrees</i>	
Surface Tilt Y	0.0333	<i>degrees</i>	
Spherical and Astigmatism Irregularity	0.5	<i>fringes</i>	
Element Decenter X	0.2	<i>mm</i>	
Element Decenter Y	0.2	<i>mm</i>	
Element Tilt X	0.2	<i>mm</i>	
Element Tilt Y	0.2	<i>mm</i>	
Index	0.0005		
Abbe Number	0.8	<i>%</i>	

Table 4-1 Tolerance Parameters for the DYSCO Front-End

The histogram and yield curves correspond to the tolerances relayed in Table 4-1. Tolerancing is an iterative process. The estimated performance of the as-built system will improve as tolerances are tightened. The results of the Monte Carlo analysis can best be interpreted via a histogram and yield curve (explained in their respective section).

1. Histogram

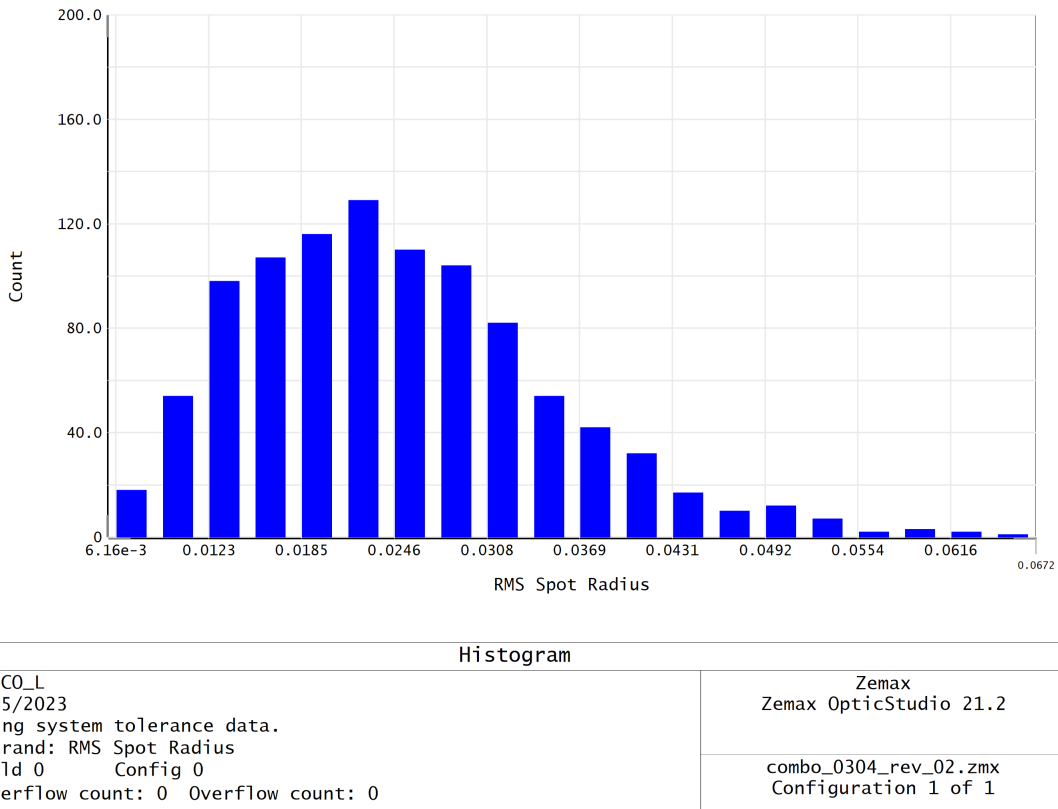


Figure 4-11 DYSCL Front-End Histogram

Figure 4-11 shows the majority of the systems will have a spot size radius of $22.4 \mu\text{m}$ or greater. An iterated tolerancing analysis would improve performance

2. Yield Curve

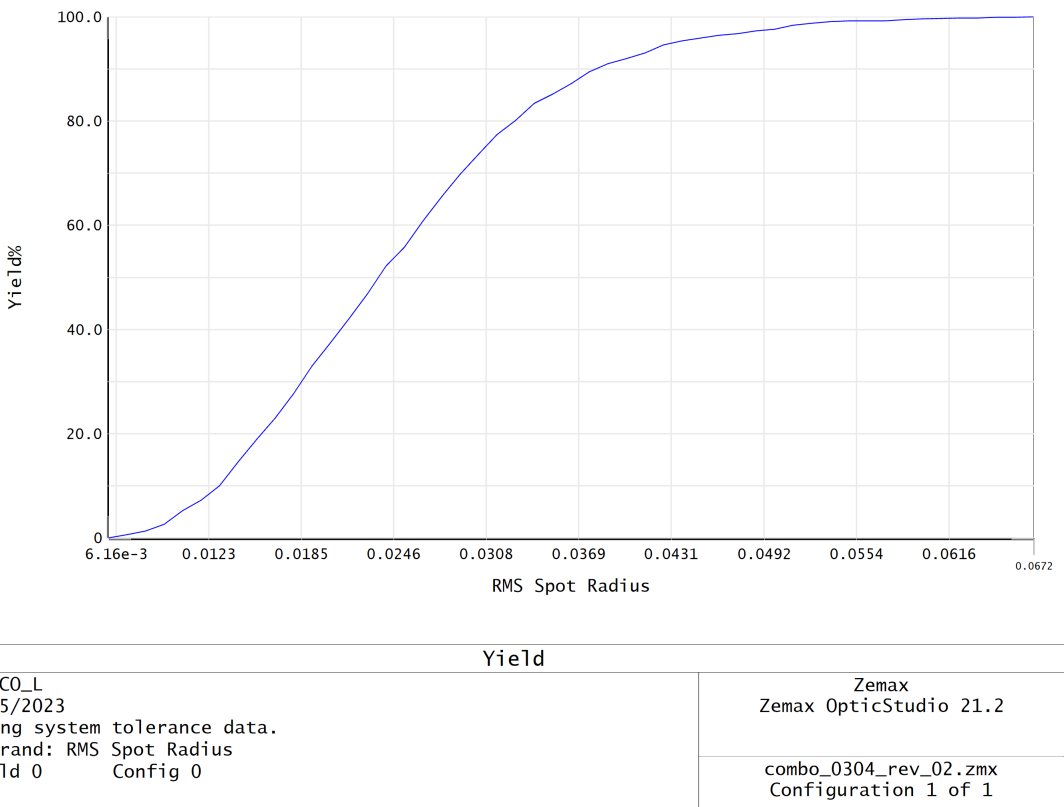


Figure 4-12 DYSCO-L Front-End Yield

Figure 4-12 shows that 90% of as built systems will have an on-axis spot size radius of 37 μm .

4.2. DYSCO Back-End

The final DYSCO back-end system has ten lens elements that include the Petzval objective and a Double Gauss derivative eyepiece.

4.2.1. *Optical Performance Metrics*

1. Layout

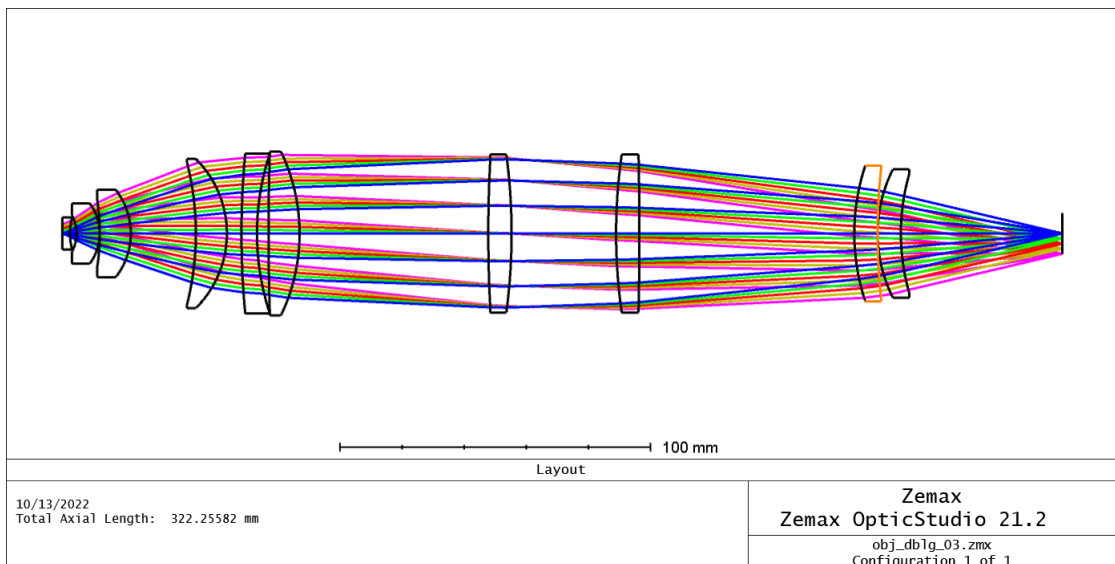


Figure 4-13 DYSCO Back-End Layout

2. Spot Size

The nominal spot size will fit well inside of the pixel size of $12.8\mu m$ with the exception of the full-field height.

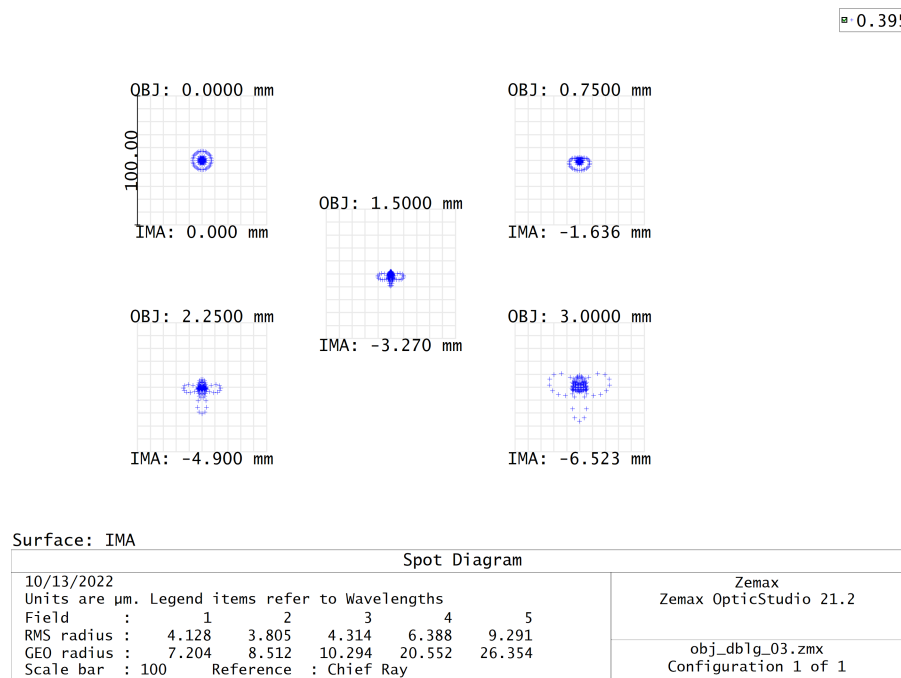
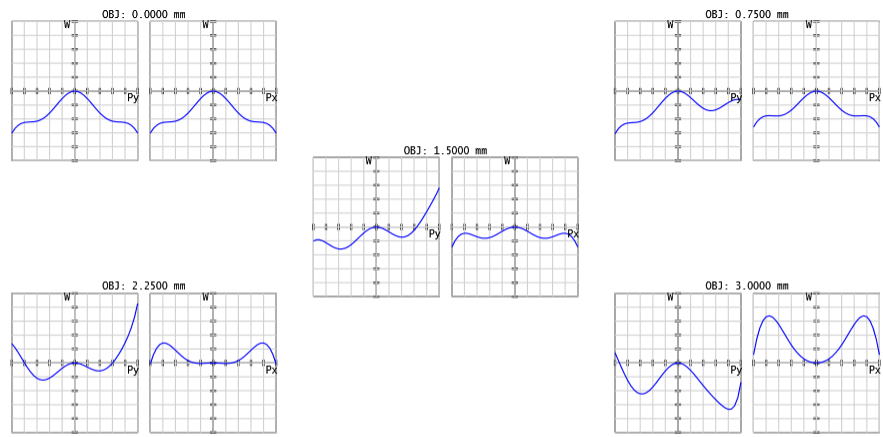


Figure 4-14 DYSCO Back-End Spot Diagram

3. Wavefront Error

One can notice the residual field curvature dominant across all field points, as seen by the quadratic behavior of the on-axis OPD fan. There is also slight coma as one goes off axis.



Optical Path Difference	
10/13/2022 Maximum Scale: ± 2.000 Waves. <u>0.395</u> Surface: Image	Zemax Zemax OpticStudio 21.2 obj_dblg_03.zmx Configuration 1 of 1

Figure 4-15 DYSCO Wavefront Error

4. Resolution

The Modulation Transfer Function (MTF) shows the contrast capability of the system at the cutoff frequency of 78 lp/mm. This cutoff frequency corresponds with the camera's pixel pitch cutoff frequency which is a greater performance than what is required to resolve the Debye-Scherrer cones.

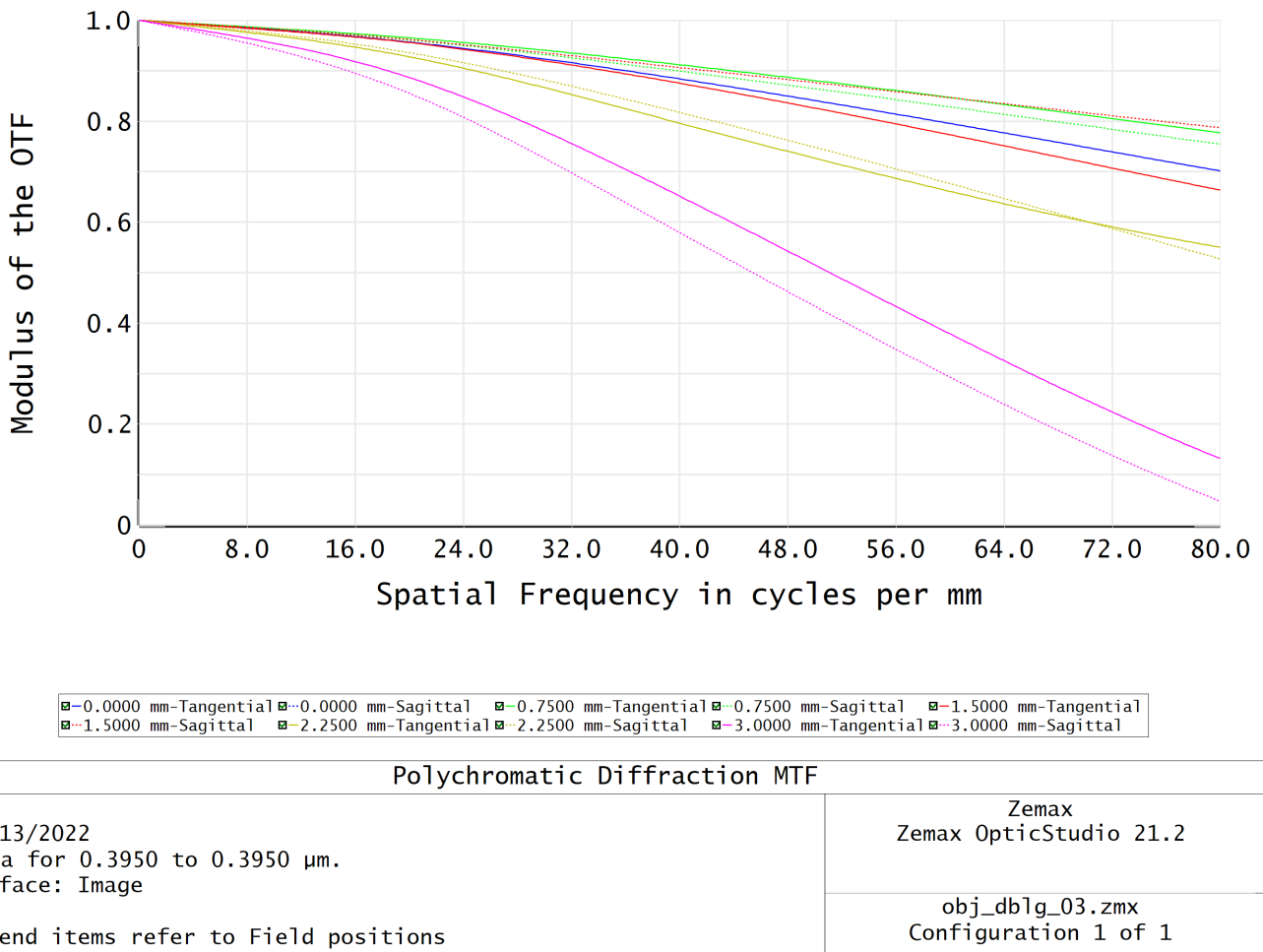


Figure 4-16 DYSCO MTF Resolution Chart

5. Image Simulations

Several Calibration targets were designed for the purpose of registering the image. The line width of the reticles is $100 \mu\text{m}$ that translates to 10mm^{-1} or 20 lp/mm for light modulation. The performance of the system as described in figure 4-16 exceeds this requirement.

4.2.2. **Tolerancing Analysis**

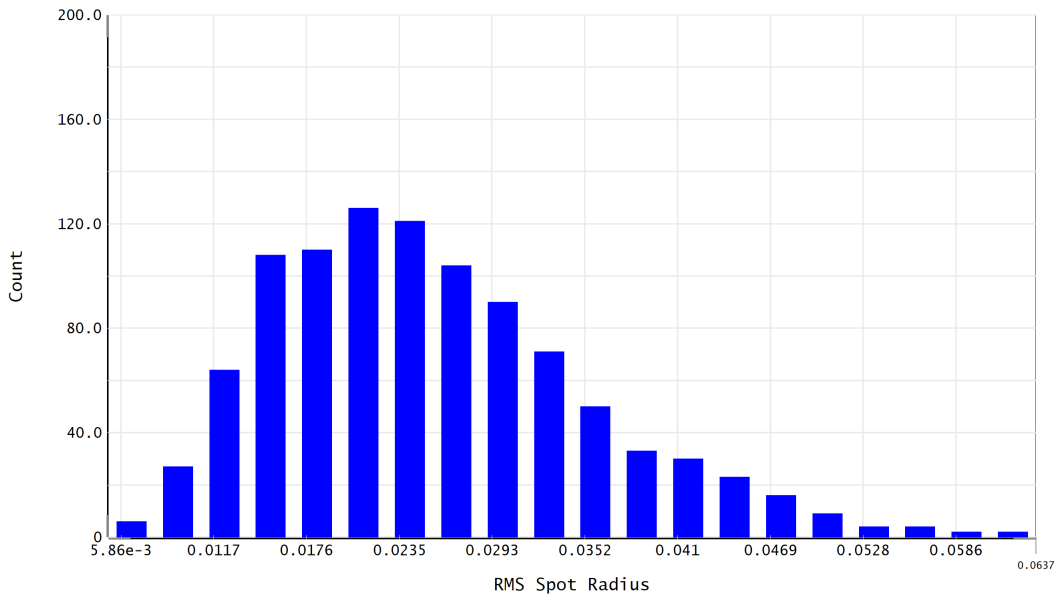
The complete tolerance list is displayed in Table 4-2.

Parameter	Values	Units	Comments
Radius	3	<i>fringes</i>	
Thickness	0.05	<i>mm</i>	
Surface Decenter X	0.2	<i>mm</i>	
Surface Decenter Y	0.2	<i>mm</i>	
Surface Tilt X	0.0333	<i>degrees</i>	
Surface Tilt Y	0.0333	<i>degrees</i>	
Spherical and Astigmatism Irregularity	0.5	<i>fringes</i>	
Element Decenter X	0.2	<i>mm</i>	
Element Decenter Y	0.2	<i>mm</i>	
Element Tilt X	0.2	<i>mm</i>	
Element Tilt Y	0.2	<i>mm</i>	
Index	0.0005		
Abbe Number	0.8	<i>%</i>	

Table 4-2 Tolerance Parameters for the DYSCO Back End

The histogram and yield curves correspond to the given values in Table 4-2.

1. Histogram



Histogram	
1/25/2023 Using system tolerance data. Operand: RMS Spot Radius Field 0 Config 0 Underflow count: 0 Overflow count: 0	Zemax Zemax OpticStudio 21.2 obj_db1g_03.zmx Configuration 1 of 1

Figure 4-17 DYSCO Back-End Histogram

Figure 4-17 shows the majority of systems will have a spot size radius 21 μm or larger.

2. Yield Curve

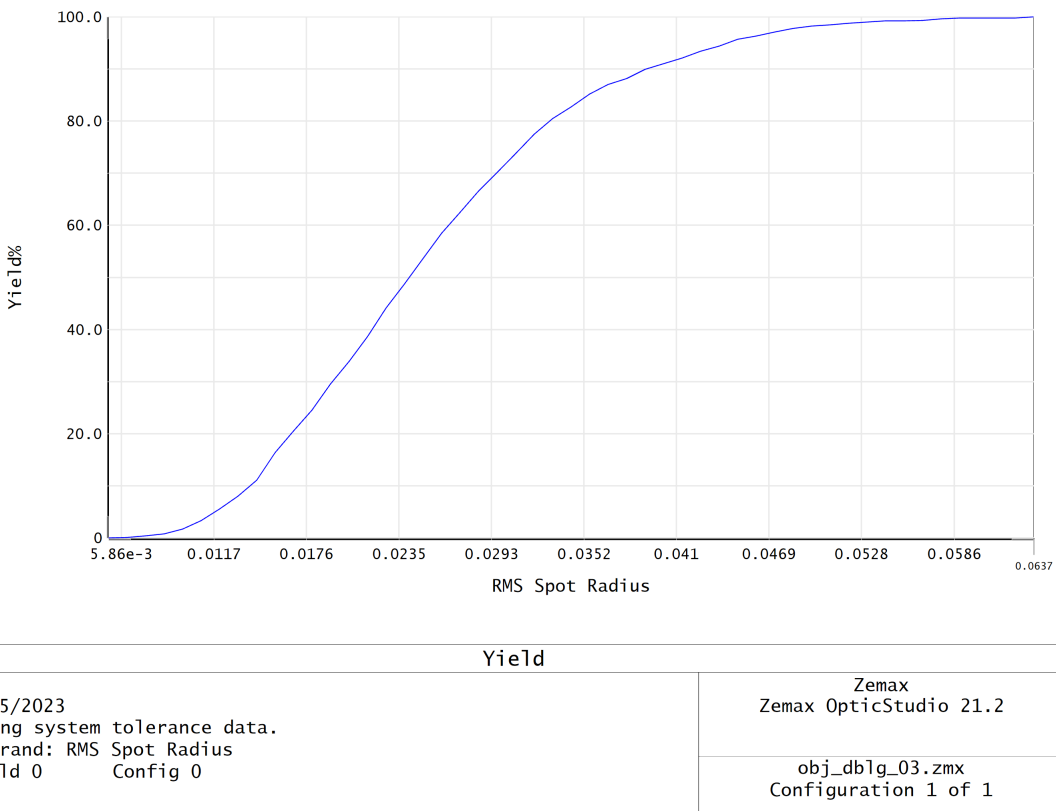


Figure 4-18 DYSCO Back-End Yield

Figure 4-18 shows that 90% of the as built systems will have a spot size radius greater than $40 \mu\text{m}$.

4.3. Radiance Characterization

The radiance profile of the scintillator is analyzed.

4.3.1. Data Capture

As described in the Methodology portion, the radiance profile of the scintillator was calculated by capturing images of the scintillator at several angles of incidence. The basic radiometer would stay parallel to the optical axis and the scintillator would rotate about the field stop axis (see Figure 3-13).

4.3.2. Data Analysis

The data analysis follows Baudet closely [34]. An image was captured at every angular position (rotation angle) with a 30 second exposure time. This image was then averaged to obtain one data point. The points were then plotted on a chart, normalized to unity, and compared against a cosine plot. The Lambertian nature of the scintillator would be proved when the irradiance vs rotation angle matched the cosine plot. While the radiance profile of the ‘Fast Decay’ (Fig 4-20), is closer to Lambertian (as the curve closely follows the cosine plot for small angles of incidence), the radiance profile of both do not match the cosine plot directly for larger angles of incidence. This implies the scintillators do not have a Lambertian behavior for all angles of incidence. This behavior may be explained by Total Internal Reflectance (TIR) occurring inside the glass substrate for the large angles of incidence.

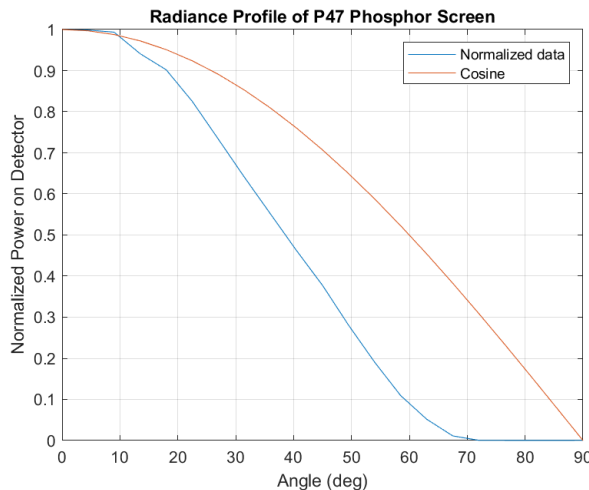


Figure 4-19 Irradiance data of the P47 scintillator as compared to the cosine curve.

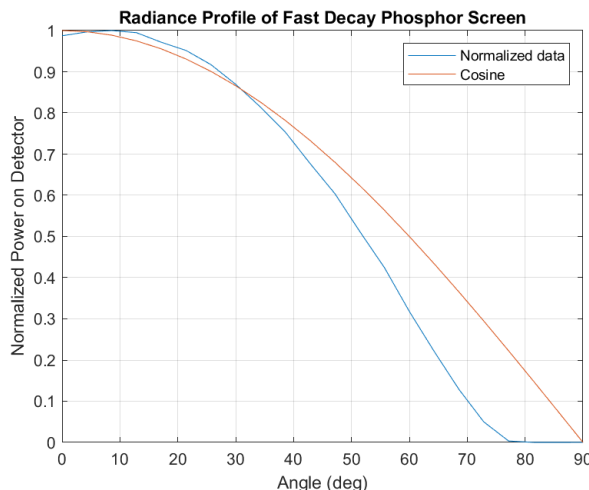


Figure 4-20 Irradiance data of the Fast Decay scintillator as compared to the cosine curve.

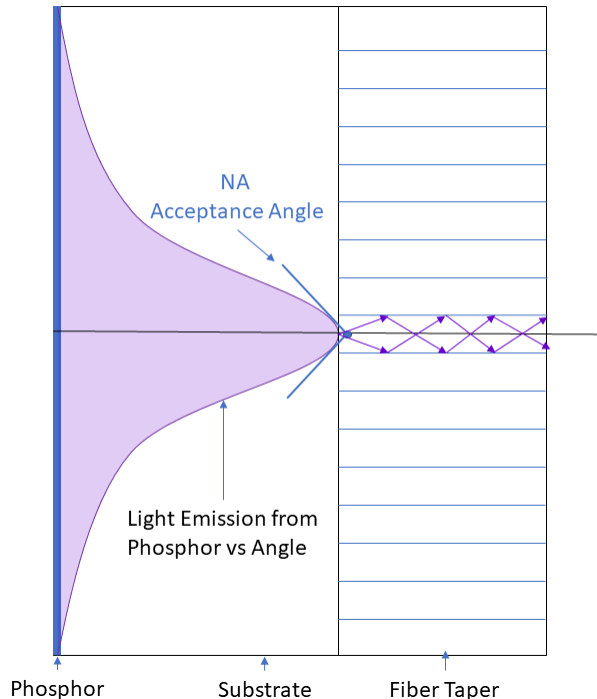


Figure 4-21 Light-fiber taper coupling showing a narrower than cosine distribution of light interacting with the fiber taper cores.

Conceptualized in Figure 4-21, more light is transmitted through the taper if the emission is narrower than Lambertian.

5. CONCLUSION

5.1. Summary of Design Work

The author has shown the design and analysis of an optical system for use in an XRD diagnostic system for dynamic compression experiments. The optical system is comprised of three distinct portions: the front-end, back-end, and imaging fiber-cable optical relay.

The front- and back-end systems were individually designed based on the patent literature and coupled together via the plastic optical fiber relay to form an excellent imaging system that exceeds optical, optomechanical, and environmental constraints. The modular nature of the DYSCO allows different scintillator and camera couplers to be used depending on the needs of the researcher. Furthermore, several front-end variants have been assembled and commissioned in the lab.

The fiber optic relay had several data processing hurdles that were addressed via a custom GUI. First, the 'rosette' nature of the super bundle did not conserve the spatial location of each pupil from entrance to exit face. Secondly, the clocking, or rotational position of each bundle was not

conserved. Both issues were addressed via a user-iterated GUI that could identify, isolate, and maneuver said pupils into a spatially comprehensible data output.

Also performed was the radiometric survey of such an XRD diagnostic. From the X-ray conversion efficiency of the scintillator, to the transmission of the fiber, to the transmission of the coated optical systems, a thorough estimate of the final system's overall throughput is provided.

Finally, a definitive experiment has been conducted based on previous work by Baudet that shows the radiance profile of the scintillator to have Lambertian properties around a central subset of angles around the normal.

5.2. Future Work

- The DYSCO-L variant of the diagnostic is scheduled to be fielded on Z shortly after the submission of this thesis.
- The ‘DYSCO-Straight’ variant of this diagnostic will be fielded at the Dynamic Compression Sector facility.
- Various commissioning experiments of all both front-end variants will be performed at the Z-Beamlet facility next door to the Z Machine Pulsed Power facility in Albuquerque, New Mexico.
- The back-end portion of DYSCO will need to be manufactured, assembled, and tested.
- An optical fiber coupler has been designed but not analyzed nor manufactured to reduce plastic optical fiber waste upon every shot. Currently, the whole fiber is consumed every shot. If two fibers were optically coupled together at the vacuum port of the Z Machine, waste would be reduced.
- A monolithic fiber option is being pursued. This would negate the need for the GUI.

5.3. Impact on Z Diagnostics

Ultimately, DYSCO and its predecessor, DISCO, represent a unique diagnostic capability within the Z Containment context that allows X-ray diffraction work to continue even in challenging optomechanical environments. The first-generation DISCO allowed capture of XRD data away from the camera sensor. This enabled the camera to be placed inside a shielded box during a Z experiment (‘shot’) while the front-end and fiber portions were consumed. The second-generation DYSCO and its front-end variants allow potential containment-compatible fielding and data acquisition.

REFERENCES

- [1] E S Dana. *A Textbook of Mineralogy with an Extended Treatise on Crystallography and Physical Mineralogy*. John Wiley and Sons, 1922.
- [2] Carolyn MacDonald. An introduction to x-ray physics, optics, and applications. In *An Introduction to X-Ray Physics, Optics, and Applications*. Princeton University Press, 2017.
- [3] Martin Etter and Robert E Dinnebier. A century of powder diffraction: a brief history. *Zeitschrift für anorganische und allgemeine Chemie*, 640(15):3015–3028, 2014.
- [4] P. W. Bridgman. Recent work in the field of high pressures. *Rev. Mod. Phys.*, 18:1–93, Jan 1946.
- [5] Ho G Drickamer. The effect of high pressure on the electronic structure of solids. In *Solid State Physics*, volume 17, pages 1–133. Elsevier, 1965.
- [6] Stanley Block and Gasper Piermarini. The diamond cell stimulates high-pressure research. *Physics Today*, 29(9):44–55, 1976.
- [7] A. Jayaraman. Diamond anvil cell and high-pressure physical investigations. *Rev. Mod. Phys.*, 55:65–108, Jan 1983.
- [8] RH Wentorf Jr. Modern very-high-pressure research. *British Journal of Applied Physics*, 18(7):865, 1967.
- [9] Lee Davison and R.A Graham. Shock compression of solids. *Physics Reports*, 55(4):255–379, 1979.
- [10] Amy Lazicki, JR Rygg, Federica Coppari, Ray Smith, Dayne Fratanduono, RG Kraus, GW Collins, R Briggs, DG Braun, DC Swift, et al. X-ray diffraction of solid tin to 1.2 tpa. *Physical review letters*, 115(7):075502, 2015.
- [11] DH Kalantar, JF Belak, GW Collins, JD Colvin, HM Davies, JH Eggert, TC Germann, J Hawreliak, BL Holian, K Kadau, et al. Direct observation of the α - ϵ transition in shock-compressed iron via nanosecond x-ray diffraction. *Physical Review Letters*, 95(7):075502, 2005.
- [12] Adrien Denoeud, Norimasa Ozaki, Alessandra Benuzzi-Mounaix, Hiroyuki Uranishi, Yoshihiko Kondo, Ryosuke Kodama, Erik Brambrink, Alessandra Ravasio, Maimouna Bocoum, Jean-Michel Boudenne, et al. Dynamic x-ray diffraction observation of shocked solid iron up to 170 gpa. *Proceedings of the National Academy of Sciences*, 113(28):7745–7749, 2016.
- [13] LM Barker and RE Hollenbach. Laser interferometer for measuring high velocities of any reflecting surface. *Journal of Applied Physics*, 43(11):4669–4675, 1972.
- [14] J. R. Rygg, J. H. Eggert, A. E. Lazicki, F. Coppari, J. A. Hawreliak, D. G. Hicks, R. F. Smith, C. M. Sorce, T. M. Uphaus, B. Yaakobi, and G. W. Collins. Powder diffraction from solids in the terapascal regime. *Review of Scientific Instruments*, 83(11):113904, 2012.

- [15] J. R. Rygg, R. F. Smith, A. E. Lazicki, D. G. Braun, D. E. Fratanduono, R. G. Kraus, J. M. McNamey, D. C. Swift, C. E. Wehrenberg, F. Coppari, M. F. Ahmed, M. A. Barrios, K. J. M. Blobaum, G. W. Collins, A. L. Cook, P. Di Nicola, E. G. Dzenitis, S. Gonzales, B. F. Heidl, M. Hohenberger, A. House, N. Izumi, D. H. Kalantar, S. F. Khan, T. R. Kohut, C. Kumar, N. D. Masters, D. N. Polsin, S. P. Regan, C. A. Smith, R. M. Vignes, M. A. Wall, J. Ward, J. S. Wark, T. L. Zobrist, A. Arsenlis, and J. H. Eggert. X-ray diffraction at the national ignition facility. *Review of Scientific Instruments*, 91(4):043902, 2020.
- [16] Introduction to the aps, overview. Available at
<https://www.aps.anl.gov/About/Overview> (2023/02/21).
- [17] N. W. Sinclair, S. J. Turneaure, Y. Wang, K. Zimmerman, and Y. M. Gupta. The fast multi-frame X-ray diffraction detector at the Dynamic Compression Sector. *Journal of Synchrotron Radiation*, 28(4):1216–1228, Jul 2021.
- [18] Timothy J. Madden, William McGuigan, Michael J. Molitsky, Istvan Naday, Alan McArthur, and Edwin M. Westbrook. Lens-coupled ccd detector for x-ray crystallography. In *2006 IEEE Nuclear Science Symposium Conference Record*, volume 2, pages 729–734, 2006.
- [19] D. B. Sinars, M. A. Sweeney, C. S. Alexander, D. J. Ampleford, T. Ao, J. P. Apruzese, C. Aragon, D. J. Armstrong, K. N. Austin, T. J. Awe, A. D. Baczewski, J. E. Bailey, K. L. Baker, C. R. Ball, H. T. Barclay, S. Beatty, K. Beckwith, K. S. Bell, J. F. Benage, N. L. Bennett, K. Blaha, D. E. Bliss, J. J. Boerner, C. J. Bourdon, B. A. Branch, J. L. Brown, E. M. Campbell, R. B. Campbell, D. G. Chacon, G. A. Chandler, K. Chandler, P. J. Christenson, M. D. Christison, E. B. Christner, R. C. Clay, K. R. Cochrane, A. P. Colombo, B. M. Cook, C. A. Coverdale, M. E. Cuneo, J. S. Custer, A. Dasgupta, J.-P. Davis, M. P. Desjarlais, D. H. Dolan, J. D. Douglass, G. S. Dunham, S. Duwal, A. D. Edens, M. J. Edwards, E. G. Evstatiev, B. G. Farfan, J. R. Fein, E. S. Field, J. A. Fisher, T. M. Flanagan, D. G. Flicker, M. D. Furnish, B. R. Galloway, P. D. Gard, T. A. Gardiner, M. Geissel, J. L. Giuliani, M. E. Glinsky, M. R. Gomez, T. Gomez, G. P. Grim, K. D. Hahn, T. A. Haill, N. D. Hamlin, J. H. Hammer, S. B. Hansen, H. L. Hanshaw, E. C. Harding, A. J. Harvey-Thompson, D. Headley, M. C. Herrmann, M. H. Hess, C. Highstrete, O. A. Hurricane, B. T. Hutsel, C. A. Jennings, O. M. Johns, D. Johnson, M. D. Johnston, B. M. Jones, M. C. Jones, P. A. Jones, P. E. Kalita, R. J. Kamm, J. W. Kellogg, M. L. Kiefer, M. W. Kimmel, P. F. Knapp, M. D. Knudson, A. Kreft, G. R. Laity, P. W. Lake, D. C. Lamppa, W. L. Langston, J. S. Lash, K. R. LeChien, J. J. Leckbee, R. J. Leeper, G. T. Leifeste, R. W. Lemke, W. Lewis, S. A. Lewis, G. P. Loisel, Q. M. Looker, A. J. Lopez, D. J. Lucero, S. A. MacLaren, R. J. Magyar, M. A. Mangan, M. R. Martin, T. R. Mattsson, M. K. Matzen, A. J. Maurer, M. G. Mazarakis, R. D. McBride, H. S. McLean, C. A. McCoy, G. R. McKee, J. L. McKenney, A. R. Miles, J. A. Mills, M. D. Mitchell, N. W. Moore, C. E. Myers, T. Nagayama, G. Natoni, A. C. Owen, S. Patel, K. J. Peterson, T. D. Pointon, J. L. Porter, A. J. Porwitzky, S. Radovich, K. S. Raman, P. K. Rambo, W. D. Reinhart, G. K. Robertson, G. A. Rochau, S. Root, D. V. Rose, D. C. Rovang, C. L. Ruiz, D. E. Ruiz, D. Sandoval, M. E. Savage, M. E. Sceiford, M. A. Schaeuble, P. F. Schmit, M. S. Schollmeier, J. Schwarz, C. T. Seagle, A. B. Sefkow, D. B. Seidel, G. A. Shipley, J. Shores, L. Shulenburger, S. C. Simpson, S. A. Slutz, I. C. Smith, C. S. Speas, P. E. Specht, M. J. Speir, D. C. Spencer, P. T. Springer, A. M. Steiner, B. S. Stoltzfus, W. A. Stygar, J. Ward Thornhill, J. A. Torres, J. P. Townsend, C. Tyler, R. A.

- Vesey, P. E. Wakeland, T. J. Webb, E. A. Weinbrecht, M. R. Weis, D. R. Welch, J. L. Wise, M. Wu, D. A. Yager-Elorriaga, A. Yu, and E. P. Yu. Review of pulsed power-driven high energy density physics research on z at sandia. *Physics of Plasmas*, 27(7):070501, 2020.
- [20] Tommy Ao, Anthony Smith, Matthias Geissel, Mark W Kimmel, Paul D Gard, and Marius Schollmeier. Evaluation of a fiber-coupled x-ray diffraction detector for dynamic compression experiments. Technical report, Sandia National Lab.(SNL-NM), Albuquerque, NM (United States), 2021.
- [21] T. Ao, M. Schollmeier, P. Kalita, P. D. Gard, I. C. Smith, J. E. Shores, C. S. Speas, and C. T. Seagle. A spherical crystal diffraction imager for sandia's z pulsed power facility. *Review of Scientific Instruments*, 91(4):043106, 2020.
- [22] Vitalij. Pecharsky, Peter. Zavalij, and Schweizerische Nationalliga fur Krebsbekampfung und Krebsforschung. *Fundamentals of Powder Diffraction and Structural Characterization of Materials, Second Edition*. Springer, 2nd ed. 2009. edition, 2009. Includes bibliographical references and index.
- [23] Tommy Ao, Brendan Donohoe, Carianne Martinez, Marcus Knudson, David Montes de Oca Zapiain, Dane Morgan, Mark Rodriguez, and James Lane. Ldrd 226360 final project report: Simulated x-ray diffraction and machine learning for optimizing dynamic experiment analysis. 10 2022.
- [24] Hugh D Young, Roger A Freedman, and A Lewis Ford. *University Physics with Modern Physics*. Pearson Education, 2013.
- [25] RW Lemke, MD Knudson, DE Bliss, K Cochrane, J-P Davis, AA Giunta, HC Harjes, and SA Slutz. Magnetically accelerated, ultrahigh velocity flyer plates for shock wave experiments. *Journal of Applied Physics*, 98(7):073530, 2005.
- [26] JR Asay, T Ao, J-P Davis, C Hall, TJ Vogler, and GT Gray III. Effect of initial properties on the flow strength of aluminum during quasi-isentropic compression. *Journal of Applied Physics*, 103(8):083514, 2008.
- [27] PI Dorogokupets, AM Dymshits, KD Litasov, and TS Sokolova. Thermodynamics and equations of state of iron to 350 gpa and 6000 k. *Scientific reports*, 7(1):1–11, 2017.
- [28] Tomokazu Sano, Hiroaki Mori, Etsuji Ohmura, and Isamu Miyamoto. Femtosecond laser quenching of the ϵ phase of iron. *Applied physics letters*, 83(17):3498–3500, 2003.
- [29] Martin Nikl. Scintillation detectors for x-rays. *Measurement Science and Technology*, 17(4):R37, 2006.
- [30] Miles N Wernick and John N Aarsvold. *Emission tomography: the fundamentals of PET and SPECT*. Elsevier, 2004.
- [31] A Lempicki, AJ Wojtowicz, and E Berman. Fundamental limits of scintillator performance. *Nuclear Instruments and Methods in Physics Research Section A: Accelerators, Spectrometers, Detectors and Associated Equipment*, 333(2-3):304–311, 1993.
- [32] James M. Palmer and Barbara G Grant. *The Art of Radiometry*. SPIE Press, 2010.

- [33] Cornelius J. Willers. *Electro-Optical System Analysis and Design: A Radiometry Perspective*. SPIE Press, 2013.
- [34] Camille Baudet. Radiance characterization of scintillators. Master's thesis, The University of Arizona, 2011.
- [35] Barbara Geri Grant. Field guide to radiometry. SPIE, 2011.
- [36] Kaiyuan Fan, Jun Chang, Lingjie Wang, Guangwei Shi, Hongbo Wu, and Yihan Jin. Design of fiber bundle imaging system. In Mircea Guina, Haimei Gong, Jin Lu, and Dong Liu, editors, *Optical Sensing and Imaging Technologies and Applications*, volume 10846, page 108460E. International Society for Optics and Photonics, SPIE, 2018.
- [37] José Sasián. Lecture notes in lens design, August 2021.
- [38] Milton Laikin. *Lens design*. CRC Press, 2018.
- [39] José Sasián. *Introduction to lens design*. Cambridge University Press, 2019.
- [40] Principle and transmission characteristics.
<https://www.asahi-kasei.co.jp/ake-mate/pof/en/technology/principle.html>.
accessed: 2023-03-30.
- [41] SV Borisov and NV Poberezhskaya. X-ray diffraction analysis: A brief history and achievements of the first century. *Journal of Structural Chemistry*, 53(1), 2012.
- [42] John Meurig Thomas. The birth of x-ray crystallography. *Nature*, 491(7423):186–187, 2012.
- [43] Edwin M. Westbrook, John Morse, Robert E. Fischer, William M. McGuigan, Steven K. Onishi, Paul Vu, Istvan Naday, C. Bauer, J. Phillips, T. A. Thorson, and Roger D. Durst. Design and characterization of a large-area lens-coupled CCD detector for macromolecular crystallography. In Ralph B. James, Larry A. Franks, Arnold Burger, Edwin M. Westbrook, Roger D. Durst, Edwin M. Westbrook, and Roger D. Durst, editors, *X-Ray and Gamma-Ray Detectors and Applications IV*, volume 4784, pages 375 – 385. International Society for Optics and Photonics, SPIE, 2003.
- [44] Marius Schollmeier, Tommy Ao, Ella Suzanne Field, Benjamin Robert Galloway, Patrycja E Kalita, Mark W. Kimmel, Joel Long, Dane V. Morgan, Patrick K. Rambo, Jens Schwarz, and Christopher T Seagle. X-ray diffraction measurements on laser-compressed polycrystalline samples using a short-pulse laser generated x-ray source. 9 2018.
- [45] Tommy Ao, Marius Schollmeier, Patrycja E Kalita, Paul D Gard, James Robert Williams, Caroline Bolton Blada, Heath L. Hanshaw, Ian C Smith, Jonathon Shores, Christopher Speas, and Christopher T Seagle. X-ray diffraction of dynamically compressed matter on sandia?z pulsed power facility. 10 2019.
- [46] M Schollmeier, T Ao, ES Field, BR Galloway, P Kalita, MW Kimmel, DV Morgan, PK Rambo, J Schwarz, JE Shores, et al. Polycapillary x-ray lenses for single-shot, laser-driven powder diffraction. *Review of Scientific Instruments*, 89(10):10F102, 2018.
- [47] Jerry W Forbes. *Shock wave compression of condensed matter: a primer*. Springer, 2012.

- [48] Yasuyuki Horie. *ShockWave Science and Technology Reference Library*. Springer, 2007.

APPENDIX A. DISCO GUI USER MANUAL

A.1. The File Structure

The DISCO GUI app repository ‘*disco_img_processor/*’ has many files including source code, sample raw data files, overlay target files, and end-product files. The important folders are listed below.

- MATLAB
 - Antebellum
 - * Temp
 - Reconstruction
- Output Files
- Sample Files
 - LabCaptures
 - Targets

A.2. The Main App

The main app is called ‘ManipulatePupil.mlapp’ and can be found in */Matlab/Antebellum/*. Execution is initiated by double-clicking the .mlapp or by typing...

ManipulatePupil.mlapp

...in the command window, assuming the app file is in the current working directory.

A.3. App Work-flow

A.3.1. *Prompt for overlay*

Upon app execution, the first pop-up window prompts for the overlay image to be used in image registration. The file explorer defaults to:

-/sample_Files/Targets/OS_Sims/

- Double click on the appropriate image. This image should match the magnification of the raw data capture while preserving the image dimensionality. (2K, 4K, etc)

The overlay figure will remain open but will not be used until pupil manipulation begins. Note that the overlay figure was produced by Zemax OpticStudio software. It is a simulation based on the ideal version of the Back-End optical system. Due to tolerances in assembly, the as-built performance is worse and image degradation can be present in the form of incorrect magnification and distortion. The user will notice perfect overlay is not achievable, but reasonably close. Enough spatial resolution is present to achieve a satisfactory image registration of the raw data image.

A.3.2. Load Pupil and Import Pupil sub-app

The first step is to click the ‘Load Pupils’ button in the main app which launches the Import Pupil sub application.

- Click on the ‘Import Image’ button to open a file selection window.
- Select file: ‘-/sample_Files/LabCaptures/B21012607/2mm Grid Reticle 1.tif’

The selected image will populate in the UI Axes panel. Note that the Caxis adjustment window is now activated.

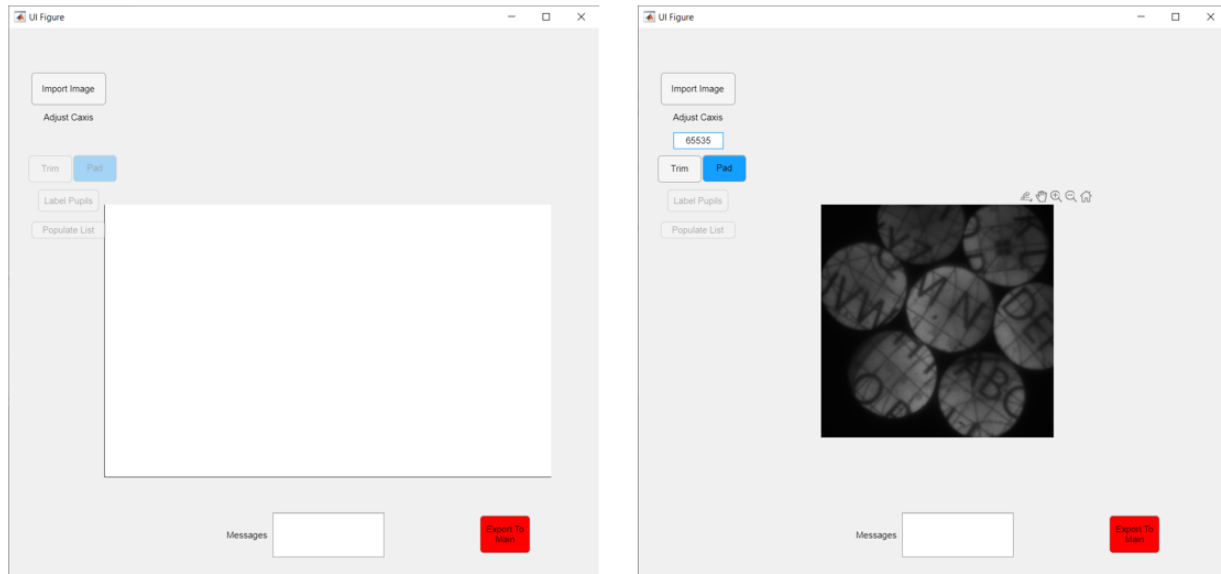


Figure A-1 Load Reticle image

A.3.3. Adjust ‘caxis’ and ‘pad’ button

To achieve useable contrast with the overlay image, a high contrast caxis limit must be chosen at this step. Note that the pupils are clipped due to the overfilling of the detector by the imaging system used. A border must be added to effectively manipulate the pupil into position. The ‘Pad’ button adds a border of infinite values around the original 1k x 1k image.

- Choose a caxis value of ‘65535’ in the caxis window
- Click ‘Pad’ button to automatically achieve a 2k x 2k image.

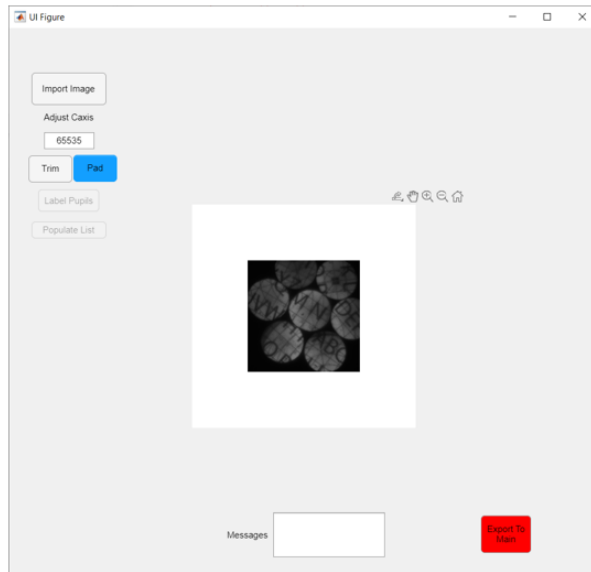


Figure A-2 Padding Image to 2048x2048

A.3.4. ‘Trim’ and ‘Draw Circle’ Buttons

The ‘trim’ button vernacular is a legacy action that squared the raw image should the aspect ratio not be 1:1. Clicking this button allows access to the ‘Find Pupil’ Panel. The ‘Find Pupil’ Panel will ideally automatically identify the pupils. Due to low contrast, the number, size, and location of identified pupils is erratic, and the automatic process cannot be trusted. The pupils must be identified manually. The ‘Draw Circle’ button will produce an external figure in which the identification process will commence.

- Click ‘Draw Circle’ to begin the manual process.
- Form a circle around the center pupil by clicking and dragging the cursor from one edge to the other
- Click ‘Save Circle’. Notice the pupil is highlighted and indexed with a number at the center of the pupil
- Click the center of the blue circle and drag it to circumscribe another pupil
- Click ‘Save Circle’ to save the next sub pupil

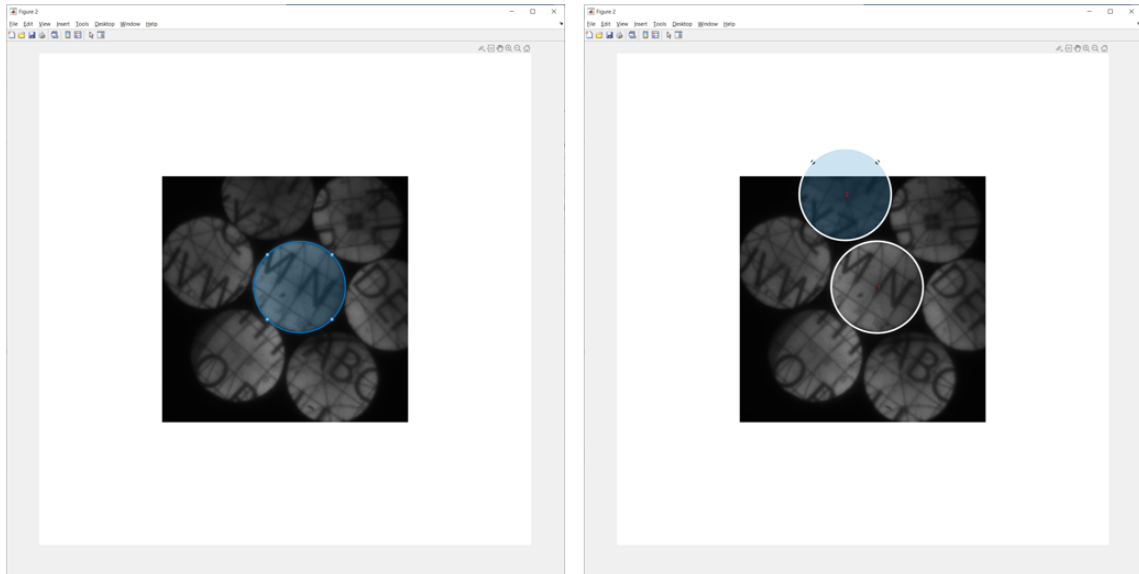


Figure A-3 Tracing pupils in process

- Drag the blue circle to the remaining pupils and click ‘Save Circle’ on each of them



Figure A-4 Completed trace of pupils

- Once all circles have been ‘saved’, click the button: ‘Export to Main’. This will automatically close the external figure. The centers and radii of the pupils are now saved
- Notice plot in the Import Pupil sub application shows labelled pupils in blue

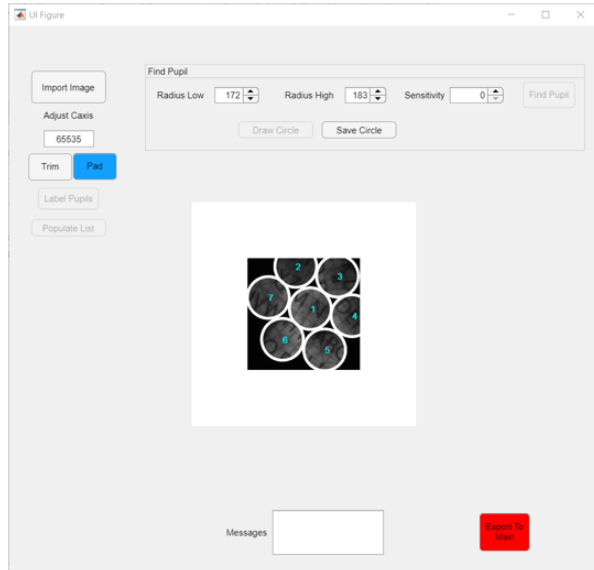


Figure A-5 Completed trace of pupils in the Import Pupil sub application

A.3.5. Main App: Selecting, Rotating and Placing Pupils

Now we begin the process of rotating and placing pupils in the correct orientation. The workflow is as follows:

1. Select a pupil from the pupil drop-down list
2. Rotate the pupil until vertical orientation is achieved and ‘locked’
3. Choose a pupil destination from the pupil drop-down list and ‘Replace’ it on the canvass
4. Move the pupil until it coincides with the corresponding location in the overlay image

A.3.6. Selecting a Pupil

After the ‘Export to Main’ button is pushed, the Main app figures will go dark. The pupil information is now loaded into this window.

- Select Pupil 1 from the drop-down menu

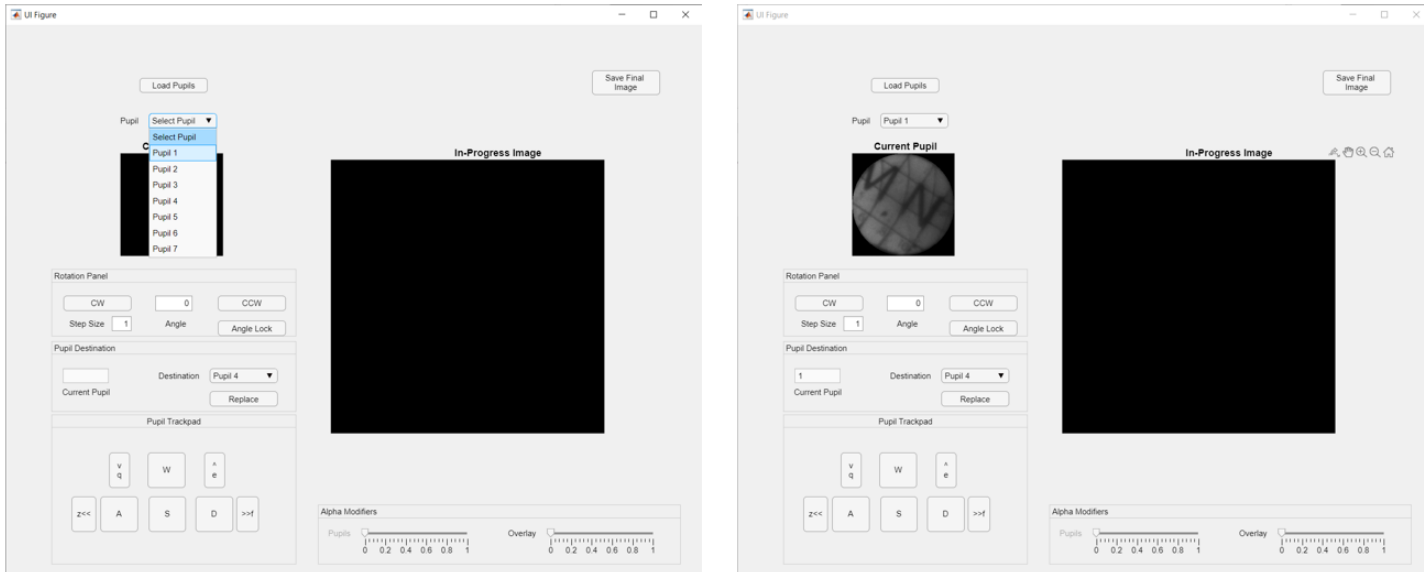


Figure A-6 Selecting pupil from drop-down menu

A.3.7. Rotate Pupil

The ‘Rotation Panel’ section has several features to aid in rotation. ‘CW’ and ‘CCW’ will rotate the pupil Clockwise or counterclockwise, respectively, by an angle amount (in degrees) specified by the ‘Step Size’ field. The ‘Angle’ field is editable and provides the option for you to guess the rotation amount.

- Enter ‘32’ in the ‘Angle’ Field
- Change step size to 0.3 and rotate using CW/CCW buttons to fine-tune rotation
- Press ‘Angle Lock’ – this saves the chosen rotation angle its corresponding pupil

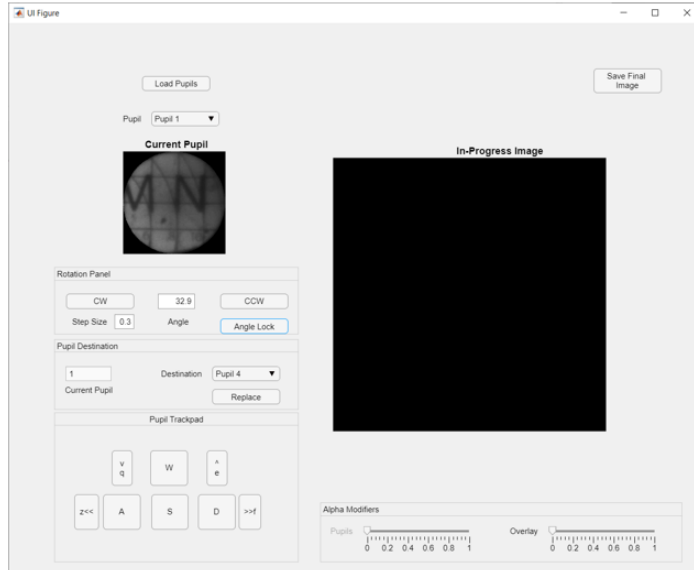


Figure A-7 Rotate pupil until upright. Note the fractional step size

A.3.8. Replace Pupil, Pupil Destination Panel, Alpha Modifiers Tab

Now that Pupil 1 has been rotated and locked, use the Overlay image and the pupil ‘map’ from the Import Pupil sub app to decide where to place Pupil 1. Upon first pressing “Replace”, the external figure will turn blank. This is corrected by modifying the Alpha value of both images using the sliders in the Alpha Modifiers panel. Since Pupil 1 shows part of ‘M’ and all of ‘N’, we will choose the Pupil 4 Location.

- Choose ‘Pupil 4’ from the Destination drop-down list
- Click ‘Replace’
- Modify the sliders in the ‘Alpha Modifiers’ Panel to achieve good contrast between images

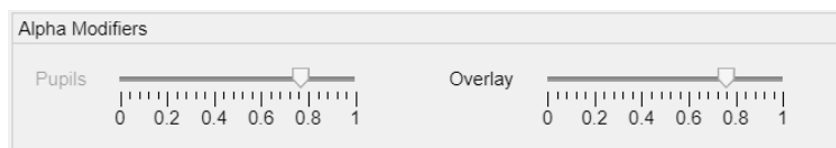


Figure A-8 Alpha Modifiers adjust the relative contrast between reticle image and overlay image

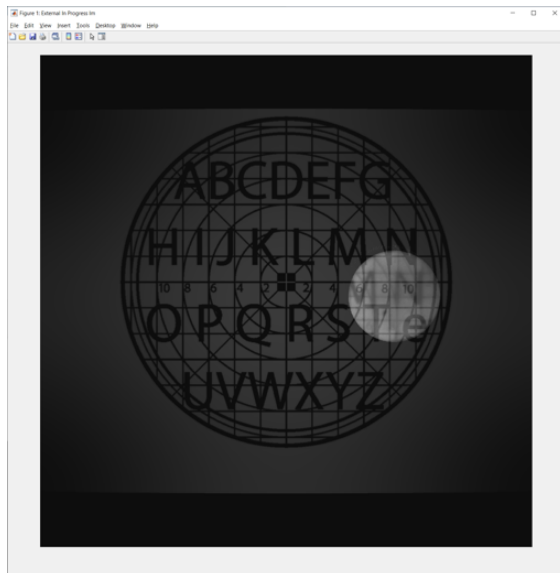


Figure A-9 Placing a pupil on the external canvass.

The pupil is now on the external canvass.

- Use “WASD” keys to maneuver pupil to the corresponding area on the overlay.
 - If there is no response, click on any gray area on the app window and try again
- Rotation can be finetuned while the pupil is on the canvass

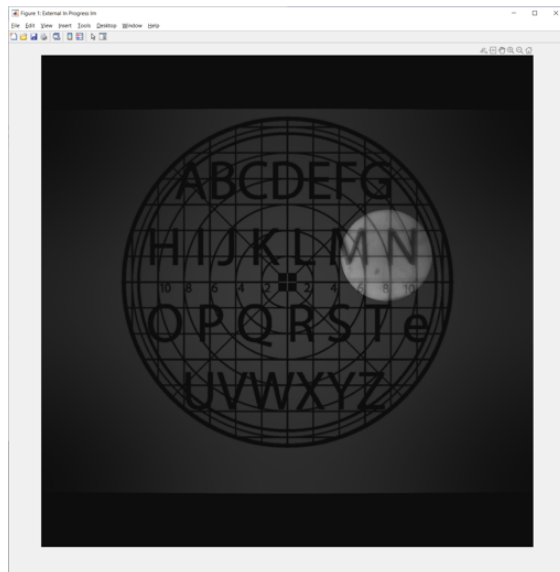


Figure A-10 Maneuver Pupil until it is co-located on top of the corresponding letters on the overlay

- Choose pupil #2 from the Pupil drop down list and repeat

A.3.9. Notes on Manipulating Pupils

When replacing subsequent pupils, pupil-to pupil overlap will occur. Not to worry, information is still stored correctly.

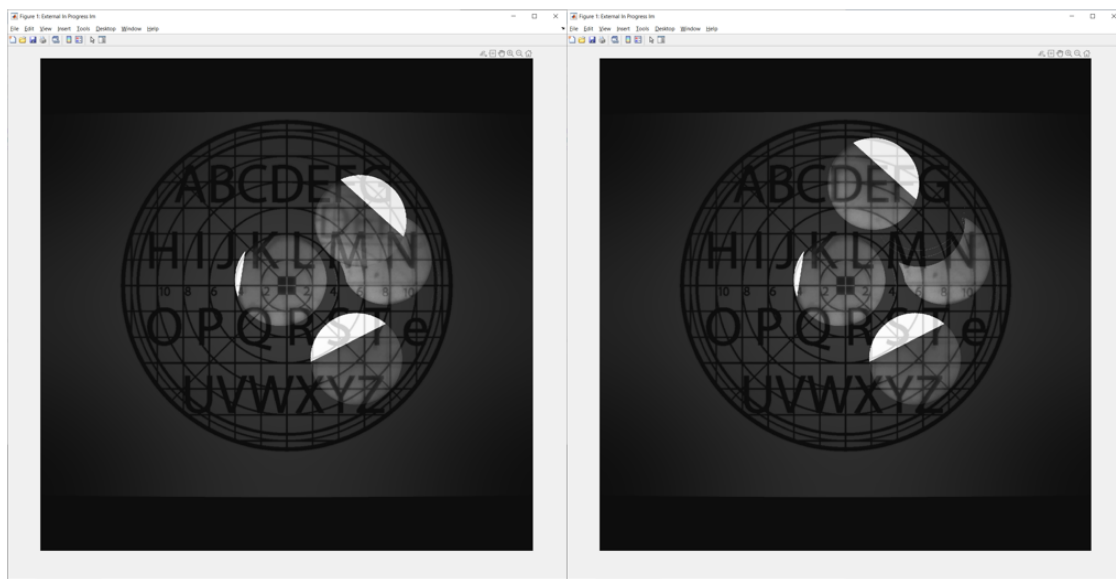


Figure A-11 Pupil overlap scenario

- choose the affected pupil fro the pupil drop-down list and ‘toggle’ the pupil by moving it one way and then back to re-plot the figure
- When pressing and holding a WASD key, residual pixels will remain on the overlay
 - Do not worry. Information is still stored correctly
 - The ‘smears’ are an artefact of plotting and will not show up on the final, saved image
- When all pupils are placed, go through the Pupil drop down list and toggle each pupil to ensure orientation is satisfactory

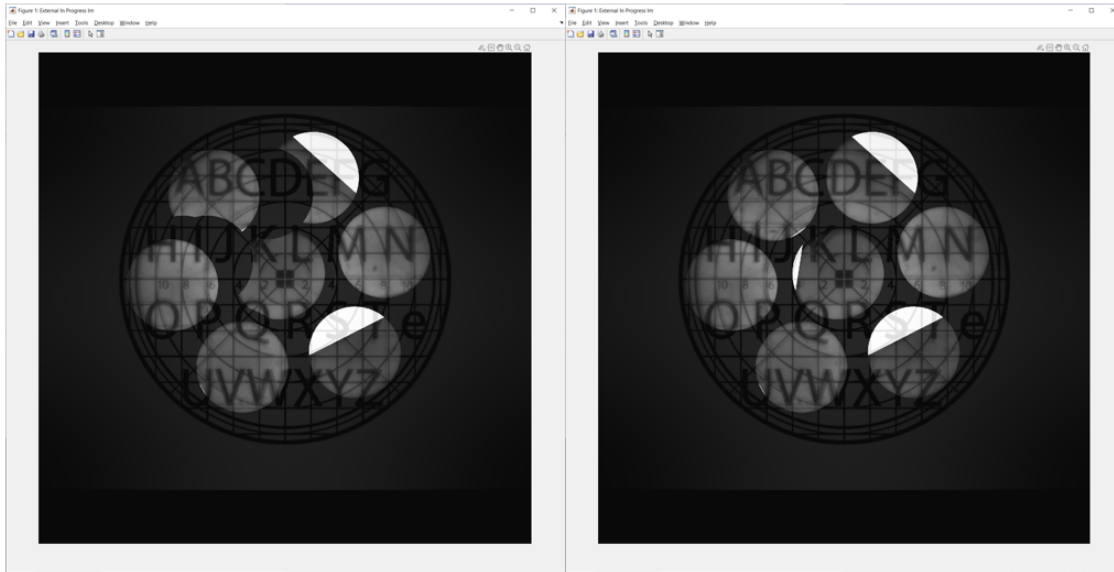


Figure A-12 Final pupil alignment onto canvass

A.3.10. *Save Final Image Button*

Once you are satisfied with the image registration, the pupil information can be saved. The current save directory is:

-/Matlab/Antebellum/Temp/

The three saved files are:

Fin_PupilBank.mat
Fin_im.tiff
Fin_ImMatrix.mat

- Click ‘Save Final Image’
- Navigate the save directory and copy/paste the results to the -/output_Files/ folder or your personal directory

A.4. Calibrating a Raw Image

Now that the Image has been registered, the calibration of the raw image can commence. The script file can be found:

-/Matlab/Reconstruction/Main_CalibrationClipped.m

The working directory should be:

-/Matlab/Reconstruction/

A.4.1. Inputs

The inputs required in the calibration script are:

1. Raw Image
 - This image is the X Ray diffraction shot to be ‘Calibrated’
 - This need not be a 2k x 2k image (2048 x 2048)
 - Shall be a grayscale of file type .tiff
2. Fin_PupilBank.mat
 - The product of the Calibration GUI. This is an array of ‘pupil’ objects that stores individual pupil decenters, rotations, and translations
3. Background Correction Image
 - This is a background image collected before the X Ray shot

A.4.2. Purpose

This file is a simple script that:

1. Pads the raw image to a 4K image size (2048 x 2048)
2. Reconstructs a pupil image based on the Fin_PupilBank.mat end-product
 - a) Construction is based on individual pupil decenters, rotations, and translations
 - b) If the construction of the pupils ‘makes sense’, the raw data product will be correct
3. Manipulates the raw data based on pupil information fields. This follows the reconstruction process described in 2.

A.4.3. Steps

- Provide raw image [.tiff]
 - Default file directory:
- /sample_Files/LabCaptures
 - Example: use B21012607/ P43-10um B210126 shot 1.tif
 - Possible file directory is the user’s personal Z shot or ZBL shot data repository for DYSCO XRD shots
- Provide pupil bank file [.mat]
 - Default file directory:

-/output_Files/Archive

- Navigate to the following to recover the latest calibration:

-/Matlab/Antebellum/Temp

- Provide Background file [.mat]
 - Unsupported as of this edition

DISTRIBUTION

Email—Internal

Name	Org.	Sandia Email Address
Tommy Ao	1646	tao@sandia.gov
Christopher Seagle	1646	ctseagl@sandia.gov
Anthony Smith	1646	asmith2@sandia.gov
Randy McKee	1690	grmckee@sandia.gov
Technical Library	1911	sanddocs@sandia.gov

Hardcopy—External

Number of Copies	Name(s)	Company Name and Company Mailing Address
1	Anthony Smith	7512 W Cosmic Sky Dr Tucson, AZ 85743



Sandia
National
Laboratories

Sandia National Laboratories is a multimission laboratory managed and operated by National Technology & Engineering Solutions of Sandia LLC, a wholly owned subsidiary of Honeywell International Inc., for the U.S. Department of Energy's National Nuclear Security Administration under contract DE-NA0003525.